JOURNAL OF GEOPHYSICAL RESEARCH: SPACE PHYSICS, VOL. 118, 5639–5658, doi:10.1002/jgra.50539, 2013

Pressure anisotropy in global magnetospheric simulations: Coupling with ring current models

X. Meng,[1] G. Tóth,[1] A. Glocer,[2] M.-C. Fok,[2] and T. I. Gombosi[1]

Received 22 January 2013; revised 10 July 2013; accepted 27 August 2013; published 12 September 2013.

[1] We have recently extended the global magnetohydrodynamic (MHD) model BATS-R-US to account for pressure anisotropy. Since the inner magnetosphere dynamics cannot be fully described even by anisotropic MHD, we coupled our anisotropic MHD model with two inner magnetospheric models: the Rice Convection Model (RCM) and the Comprehensive Ring Current Model (CRCM). The coupled models provide better representations of the near-Earth plasma, especially during geomagnetic storms. In this paper, we present the two-way coupling algorithms with both ring current models. The major difference between these two couplings is that the RCM assumes isotropic and constant pressures along closed field lines, while the CRCM resolves pitch angle anisotropy. For model validation, we report global magnetosphere simulations performed by the coupled models. The simulation results are compared to the results given by the coupled isotropic MHD and ring current models. We find that in the global MHD simulations coupled with ring current models, pressure anisotropy results in a thinner magnetosheath, a shorter tail, a much smaller Earthward plasma jet from the tail reconnection site, and is also important in controlling the magnetic field configuration. The comparisons with satellite data for the magnetospheric event simulations show improvements on reproducing the measured tail magnetic field and inner magnetospheric flow velocity when including pressure anisotropy in the ring current model coupled global MHD model.

Citation: Meng, X., G. Tóth, A. Glocer, M.-C. Fok, and T. I. Gombosi (2013), Pressure anisotropy in global magnetospheric simulations: Coupling with ring current models, *J. Geophys. Res. Space Physics*, *118*, 5639–5658, doi:10.1002/jgra.50539.

1. Introduction

[2] To take into account pressure anisotropy that has been frequently observed in the Earth's magnetosphere, for example, the inner magnetosphere [*Lui and Hamilton*, 1992; *De Michelis et al.*, 1999], the magnetosheath [*Phan et al.*, 1994], and the plasma sheet [*DeCoster and Frank*, 1979; *Takahashi and Hones*, 1988], we have extended the global MHD model BATS-R-US [*Powell et al.*, 1999] to solve for anisotropic ion pressure. To distinguish from the standard BATS-R-US with isotropic pressure, we name the new model Anisotropic BATS-R-US. The detailed description of Anisotropic BATS-R-US, particularly its validation through quiet-time magnetospheric simulations, has been presented in *Meng et al.* [2012a].

[3] Although the anisotropic MHD model is more advanced than the isotropic MHD model, it is still not appropriate in describing the inner magnetospheric dynamics. In fact, neither the isotropic nor the anisotropic MHD equations can properly capture gradient-curvature drift [*Wolf et al.*, 2009], which is energy dependent and leads to the formation of the ring current. Therefore, MHD models are not applicable to simulate various physical processes of the near-Earth plasma. A better approach is to employ kinetic models, especially during time periods of strong geomagnetic activity, when the hot ring current plasma plays an important role.

[4] Several global MHD models have been coupled with inner magnetospheric models, mainly the Rice Convection Model (RCM) [*Toffoletto et al.*, 2003] and the Comprehensive Ring Current Model (CRCM) [*Fok et al.*, 2001]. The Lyon-Fedder-Mobarry (LFM) MHD model [*Lyon et al.*, 2004] is two-way coupled with the RCM [*Toffoletto et al.*, 2004; *Pembroke et al.*, 2012]. The LFM model is also used to drive the CRCM [*Fok et al.*, 2006; *Moore et al.*, 2008]. The Open Geospace General Circulation Model (OpenGGCM) [*Raeder et al.*, 2001] is one-way coupled to RCM [*Hu et al.*, 2010]. The BATS-R-US MHD model is two-way coupled with both the RCM [*De Zeeuw et al.*, 2004] and the CRCM [*Buzulukova et al.*, 2010; *Glocer et al.*, 2013]. These coupled models successfully combine global MHD models with kinetic ring current models, providing a key step toward constructing a global general circulation model.

[5] No coupling between a global anisotropic MHD model and a ring current model has been reported to date. However, from a broader perspective of magnetospheric

[1]Department of Atmospheric, Oceanic and Space Sciences, University of Michigan, Ann Arbor, Michigan, USA.
[2]NASA Goddard Space Flight Center, Greenbelt, Maryland, USA.

Corresponding author: X. Meng, Center for Space Environment Modeling, University of Michigan, 2455 Hayward St., Ann Arbor, MI 48109, USA. (xingm@umich.edu)

2169-9380/13/10.1002/jgra.50539

modeling, equilibrium models with pressure anisotropy have been coupled to ring current models. *Zaharia et al.* [2005] fed their 3-D equilibrium code with anisotropic pressure in the equatorial plane from the UNH-RAM ring current model [*Jordanova et al.*, 1997] and analyzed the computed magnetic fields and electric fields during a geomagnetic storm. *Wu et al.* [2009] extended another equilibrium code RCM-E, which has already coupled with the RCM, to include anisotropic pressure. They also proposed the possibility of coupling the equilibrium code with the CRCM. These studies are very insightful in examining the impact of pressure anisotropy in the inner magnetosphere.

[6] In this paper we report the two-way couplings between Anisotropic BATS-R-US and both the RCM and the CRCM, which are somewhat different from the existing couplings between BATS-R-US and the two ring current models. As an extension of the standard BATS-R-US code, Anisotropic BATS-R-US belongs to the Global Magnetosphere (GM) component of the Space Weather Modeling Framework (SWMF) [*Tóth et al.*, 2012]. The Inner Magnetosphere (IM) component of the SWMF has several different models, of which the most commonly used one is the RCM. The coupling between Anisotropic BATS-R-US and the RCM is simple and straightforward, given that the coupling of the isotropic MHD version has been established already. However, since the RCM assumes pitch angle isotropy, this coupling will reduce or even eliminate pressure anisotropy in the inner magnetosphere, thus greatly limits the capability of Anisotropic BATS-R-US. Alternatively, the CRCM, another model in the IM component of the SWMF, can resolve pitch angle anisotropy. Therefore, it is more meaningful to couple Anisotropic BATS-R-US with the CRCM to obtain self-consistent solutions of pressure anisotropy throughout the whole magnetosphere. This coupling requires a new algorithm.

[7] The following content of the paper consists of four sections. In section 2, we briefly review the models involved in this study. In section 3, we describe the coupling algorithms. In section 4, we present the validation tests including idealized and storm time magnetospheric simulations. We also compare the results from the RCM and CRCM coupled models. Our conclusions are in section 5.

2. Background

2.1. Anisotropic BATS-R-US

[8] Anisotropic BATS-R-US is a three-dimensional (3-D) MHD model that solves the anisotropic MHD equations [*Meng et al.*, 2012b] under the double adiabatic approximation with an additional pressure anisotropy relaxation term based on the fire hose, mirror and ion cyclotron instability criteria, and growth rates. The primitive pressure variables in Anisotropic BATS-R-US are total pressure p and parallel pressure $p_{\parallel}$. Perpendicular pressure $p_{\perp}$ can be obtained through the relation

$$p = \frac{2p_{\perp} + p_{\parallel}}{3} \tag{1}$$

[9] Similar to the standard BATS-R-US model, when applied to simulate the global magnetosphere, Anisotropic BATS-R-US is driven by the upstream solar wind condition, which can be either idealized or real data from the ACE and WIND satellites. Due to the limited amount of solar wind thermal pressure anisotropy measurement at 1AU, our input solar wind thermal pressure is taken to be isotropic. Anisotropic BATS-R-US thus describes the pressure anisotropy arising behind the bow shock and inside the magnetosphere, as well as its global evolution with time. Anisotropic BATS-R-US also has different options for limiting pressure anisotropy. In the study presented here, we use the default option that limits the pressure anisotropy based on the growth rates of the instabilities.

2.2. RCM and CRCM

[10] Both the RCM and CRCM are kinetic models of the Earth's ring current, which is carried primarily by tens of keV ions drifting westward in the closed field line region surrounding the Earth. Both models are based on the bounce-average calculation that treats the particle distribution as a result of averaging over the particle bounce motions along the closed field lines. The underlying assumption is that the time scale of the inner magnetospheric plasma properties variation is much larger than the particle bounce periods. Furthermore, both models compute the magnetospheric electric fields self-consistently with the plasma distribution. In addition, they use similar computational grids set in the ionosphere based on longitudes and latitudes.

[11] Despite of their many common features, the RCM assumes isotropic pitch angle distribution, while the CRCM solves full pitch angle distribution. This is the major difference between the RCM and the CRCM, which results in different pictures of the inner magnetosphere. Observations have found that the ring current region is characterized by anisotropic ion and electron distributions during both quiet time and disturbed time [*Lui and Hamilton*, 1992]. Even the plasma sheet, which has long been considered to have isotropic particle distribution, contains electrons with anisotropic pitch angle distribution, according to *Walsh et al.* [2011].

3. Algorithm

[12] As the Global Magnetosphere (GM) component in the SWMF, BATS-R-US is typically coupled with the Inner Magnetosphere (IM) component and the Ionosphere Electrodynamics (IE) component to conduct geomagnetic storm simulations for the global magnetosphere. The IM component contains several ring current models including the RCM and the CRCM. The IE component is the Ridley Ionosphere Model (RIM), which is an electric potential solver [*Ridley et al.*, 2004].

[13] The general concept of the coupling between two components is to interchange variables between the two components periodically. In a typical GM-IE-IM combination, GM-IE and GM-IM are two-way coupled, while IE-IM is one-way coupled. More specifically, GM sends the field-aligned currents to IE and the magnetic field configuration to IM. IE solves for the ionospheric electric potential on a two-dimensional (2-D) height-integrated spherical surface and passes the electric potential to GM and IM. IM sends the pressure of the inner magnetosphere to GM. The three components connect together tightly by

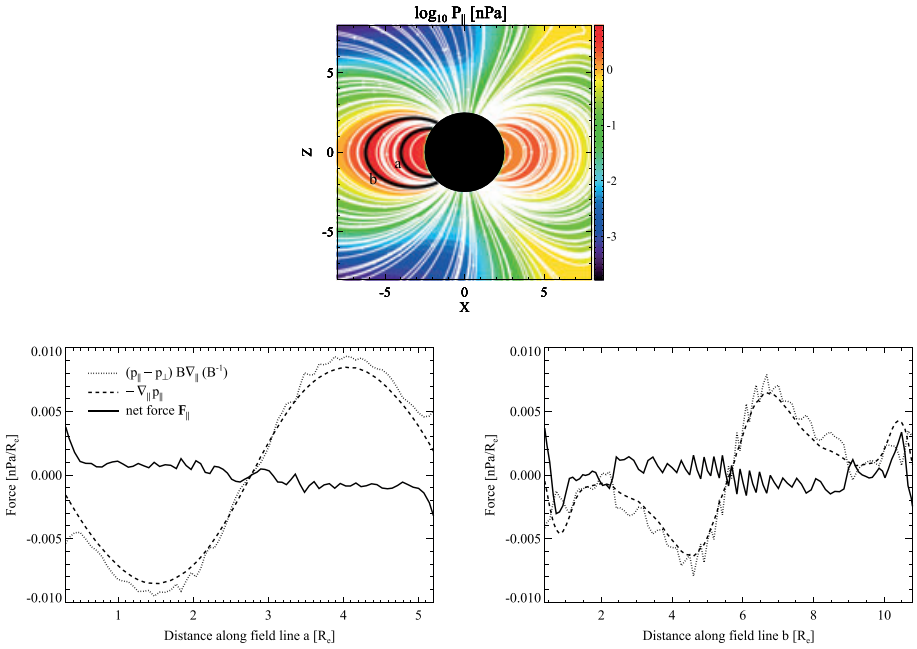

Figure 1. Force balance along the field lines for the idealized simulation with Anisotropic MHD + RIM + CRCM at time t = 4 h. (top) The logarithmic parallel pressure (colors) and the field lines (white) in the noon-midnight meridional plane from the MHD model. The black lines represent the closed field lines for which the force balance conditions are shown in the bottom plots.

the messages passed around regularly. In terms of computational efficiency, one practical task is to determine the optimal frequency of coupling one component to another, so that the states of the two components have changed significantly but not dramatically during the time interval of two successive couplings. Note that coupling parameters including the coupling frequency and the rate at which one model changes another can affect the simulation results, and optimized values are obtained based on many simulations.

[14] Although the two-way coupling algorithms between BATS-R-US and both the RCM and the CRCM have been developed [*De Zeeuw et al.*, 2004; *Glocer et al.*, 2013], these algorithms need to be modified to accommodate the coupling between Anisotropic BATS-R-US and the two ring current models.

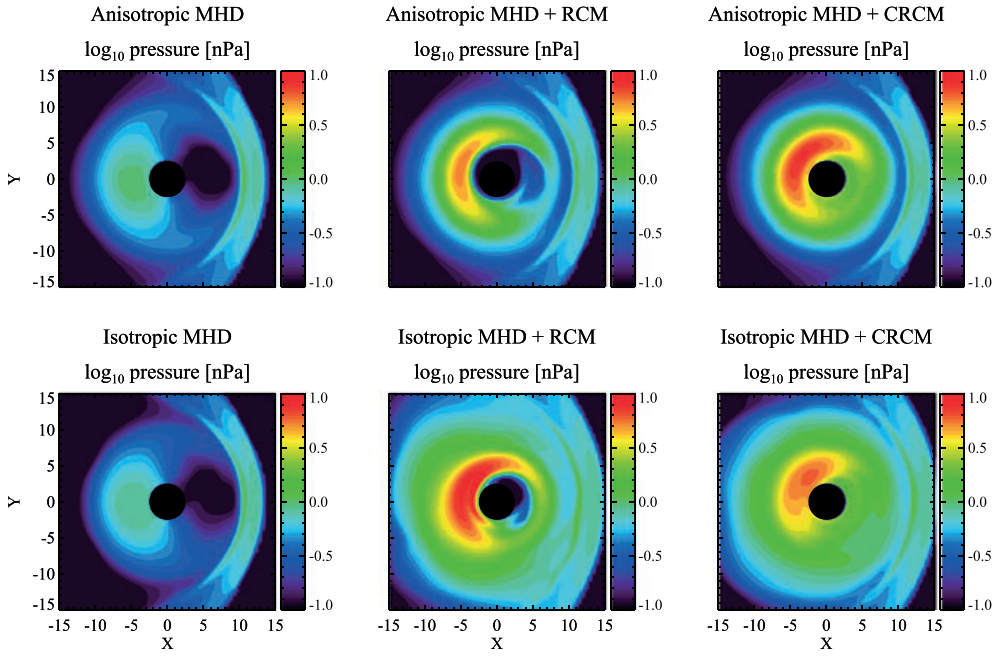

Figure 2. The logarithm of the total pressure in nPa in the equatorial (Z = 0) plane from the MHD model at t = 8 h.

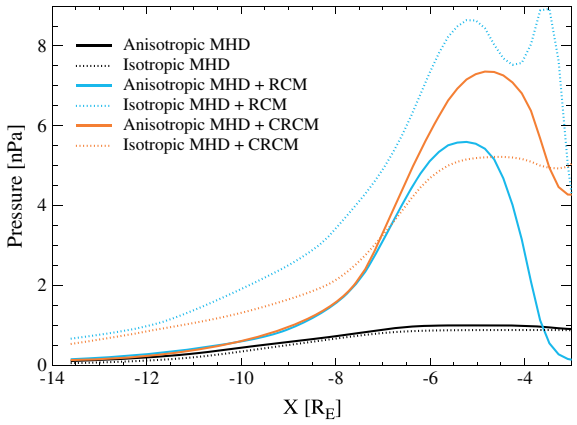

Figure 3. The nightside total pressure profile extracted along the X axis from the MHD model at t = 8 h.

3.1. Anisotropic BATS-R-US and the RCM Coupling

[15] The majority of the coupling between BATS-R-US and the RCM [*De Zeeuw et al.*, 2004] can be migrated directly to the coupling between the Anisotropic BATS-R-US and the RCM, except the pressure feedback from the RCM to BATS-R-US.

[16] The RCM computes on a 2-D longitude-latitude grid, on which closed field lines are rooted. For BATS-R-US with isotropic pressure, the RCM passes the total particle pressure (the sum of pressures of different species) for each closed field line to BATS-R-US, and the BATS-R-US pressure in every grid cell along that closed field line is nudged toward the same RCM pressure, assuming the pressure is constant along each closed field line. In Anisotropic BATS-R-US, both the parallel and total pressures along a closed field line are nudged toward the same RCM isotropic pressure for that field line, given the RCM does not resolve pressure anisotropy. This leads to a significant reduction of the pressure anisotropy in the closed field line region in Anisotropic BATS-R-US. The RCM can also provide BATS-R-US the density, which is coupled the same way as the total pressure, i.e., the BATS-R-US density along a closed field line is nudged toward the RCM density, assuming the density is constant along each closed field line. The density coupling is the same for Anisotropic BATS-R-US.

[17] The coupling between Anisotropic BATS-R-US and the RCM implants a ring current model into the global anisotropic MHD model, yet the pressure anisotropy in the inner magnetosphere cannot be completely resolved because of the pitch angle isotropy assumption in the RCM. In order to take full advantage of the anisotropic MHD model, we seek coupling with another ring current model that allows for anisotropic pressure.

3.2. Anisotropic BATS-R-US and the CRCM Coupling

[18] Recently, *Buzulukova et al.* [2010] and *Glocer et al.* [2013] introduced the CRCM into the Inner Magnetosphere component of the SWMF and implemented the one-way and two-way coupling between BATS-R-US and the CRCM, respectively. Since the CRCM can resolve pitch angle anisotropy, it can calculate the parallel and perpendicular pressure distributions in the inner magnetosphere. This provides a perfect opportunity of combining the CRCM with Anisotropic BATS-R-US to obtain self-consistent solutions of pressure anisotropy in the global magnetosphere.

[19] The two-way coupling between Anisotropic BATS-R-US and the CRCM requires a quite different algorithm from the one addressing the two-way coupling between BATS-R-US and the CRCM. In the *Glocer et al.* [2013] algorithm, BATS-R-US sends the CRCM the 3-D magnetic field configuration, and density and isotropic pressure as boundary conditions, while the CRCM feeds BATS-R-US the density and the total pressure at the magnetic equator for each closed field line. The BATS-R-US density and pressure along a closed field line are thus pushed toward the magnetic equatorial CRCM values on that field line. Same as the coupling with the RCM, the assumption of constant density and pressure along every closed field line is applied to avoid field-aligned flows in the isotropic MHD model.

[20] Anisotropic MHD, on the other hand, has a different requirement in order to maintain force balance along field lines. More specifically, the force along magnetic field can be obtained from the momentum equation [*Meng et al.*, 2012a] as

$$\begin{aligned}\mathbf{F}_{\parallel} &= \mathbf{b}\cdot\mathbf{F}\\ &= \mathbf{b}\cdot\left[\nabla\left(p_{\perp}+\frac{B^2}{2\mu_0}\right)+\nabla\cdot\left((p_{\parallel}-p_{\perp})\mathbf{bb}-\frac{\mathbf{BB}}{\mu_0}\right)\right]\\ &= (p_{\parallel}-p_{\perp})B\nabla_{\parallel}(B^{-1})+\nabla_{\parallel}p_{\parallel}\end{aligned} \tag{2}$$

where $\mathbf{b} = \mathbf{B}/|\mathbf{B}|$ and $\nabla_{\parallel} = \mathbf{b}\cdot\nabla$. In the case of MHD with isotropic pressure, (2) is simply $\nabla_{\parallel}p$, which is zero with our assumption of no pressure gradient along the magnetic field. If the pressure is anisotropic, the first term of the final expression in (2), which basically describes a mirror force, i.e., adiabatic focusing, has to be balanced by the parallel

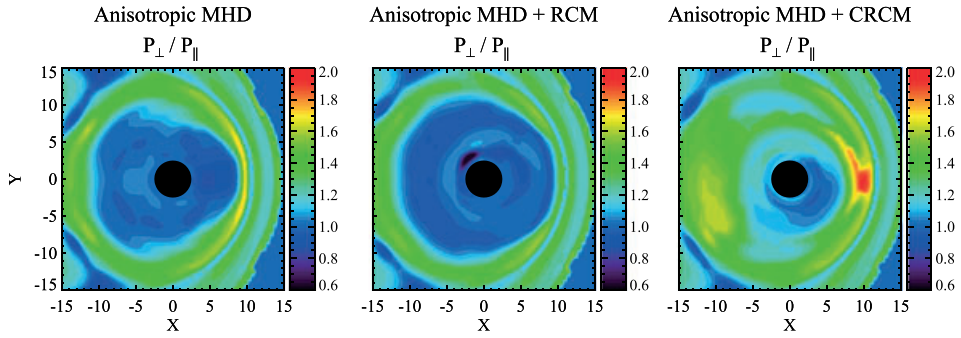

Figure 4. Pressure anisotropy ratio in the X = 0 plane from the MHD model at t = 8 h.

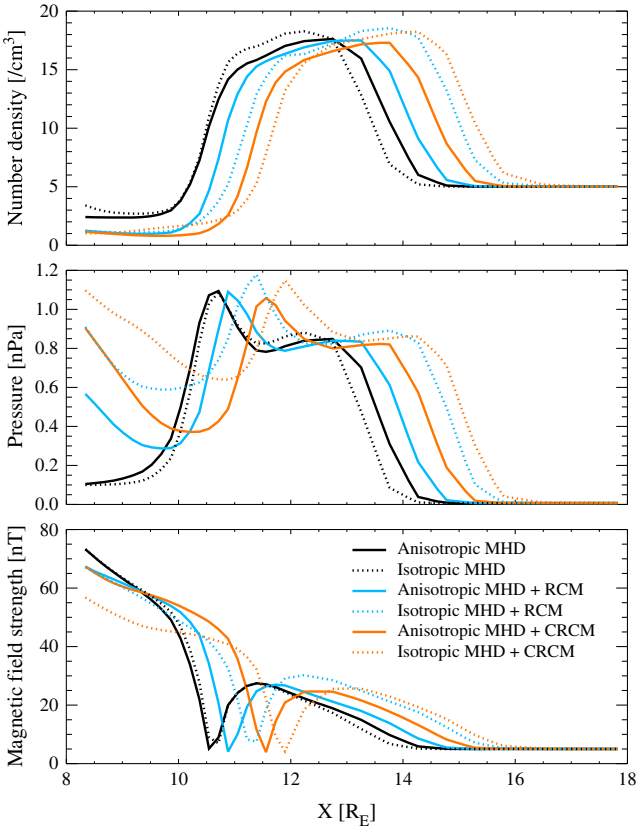

Figure 5. (top) The magnetosheath number density, (middle) total pressure and (bottom) magnetic field strength profiles extracted along the *X* axis from the MHD model at $t = 8$ h.

pressure gradient along the magnetic field. Otherwise the non-zero force will result in flows moving along closed field lines in the anisotropic MHD solutions.

[21] Bearing the pressure gradient requirement in mind, we look for an efficient coupling algorithm connecting Anisotropic BATS-R-US and the CRCM. A natural approach would be to pass the pressure distributions along each closed field line from the CRCM to Anisotropic BATS-R-US. Although this is doable, it is computationally expensive as it requires additional arrays to be passed between the two components that store the pressure values and their locations along field lines. In addition, the parallel and total pressures obtained in the CRCM do not necessarily satisfy the force balance condition in the anisotropic MHD model. To reduce the amount of information exchanged between the two models and maintain force balance in Anisotropic BATS-R-US, we build the algorithm based on Liouville's Theorem with the conservation of the first adiabatic invariant and energy, so the density and pressure profiles along magnetic field lines can be obtained from equatorial values following *Spence et al.* [1987], *Olsen et al.* [1994], *Liemohn* [2003], and *Xiao and Feng* [2006] as shown in Appendix A.

[22] The two-way coupling consists of two parts. On the one hand, Anisotropic BATS-R-US sends the magnetic field information to the CRCM. Also, the CRCM uses the density and pressures (parallel pressure and total pressure) at the minimum magnetic field point on each closed field line from Anisotropic BATS-R-US as boundary conditions to construct a bi-Maxwellian distribution at the outer boundary, i.e., the farthest closed field lines from the Earth within an ellipse, the size and position of which varies in different simulations. On the other hand, the CRCM passes Anisotropic BATS-R-US the density, the parallel and total pressures computed at the minimum magnetic field point of every closed field line, which are used by Anisotropic BATS-R-US to derive the density and pressures at "non-minimum B" locations along the closed field lines according to the following relations (see Appendix A for a derivation).

$$n_\lambda = \frac{n_0}{p_{\perp 0}/p_{\parallel 0} + B_0/B_\lambda (1 - p_{\perp 0}/p_{\parallel 0})} \tag{3}$$

$$p_{\parallel\lambda} = \frac{p_{\parallel 0}}{p_{\perp 0}/p_{\parallel 0} + B_0/B_\lambda (1 - p_{\perp 0}/p_{\parallel 0})} \tag{4}$$

$$p_{\perp\lambda} = \frac{p_{\perp 0}}{[p_{\perp 0}/p_{\parallel 0} + B_0/B_\lambda (1 - p_{\perp 0}/p_{\parallel 0})]^2} \tag{5}$$

The subscript 0 denotes the location of the minimum magnetic field on a closed field line, and λ indexes an arbitrary point along that field line. The relation (1) is employed to calculate the corresponding total pressure p_λ. Substituting equations (4) and (5) into equation (2) gives $\mathbf{F}_{\parallel\lambda} = 0$ (also shown in Appendix A), therefore the pressure distributions obey the force balance condition along the magnetic field lines.

[23] The derivation of equations (3)–(5) is based on two assumptions. First, there is no potential drop between the "minimum B" point and the point at latitude λ along the field line. Second, the distribution function at the "minimum B" point is a function of $v_\parallel^2/T_\parallel + v_\perp^2/T_\perp$, where $v_\parallel$ and $v_\perp$ are the parallel and perpendicular velocities, and $T_\parallel$, and $T_\perp$ are the parallel and perpendicular temperatures, respectively. This means that the relations are satisfied for a variety of distribution functions, including bi-Maxwellian and bi-Kappa distributions, that are reasonable approximations of the particle distribution in the inner magnetosphere.

4. Global Magnetospheric Simulations

[24] To validate Anisotropic BATS-R-US and its couplings with the two ring current models RCM and CRCM, we perform global magnetospheric simulations and analyze the differences between the anisotropic MHD and isotropic MHD simulations, as well as the differences between the RCM and the CRCM coupled simulations. We also report the comparison of the geomagnetic storm simulations to data.

4.1. Idealized Magnetosphere

[25] We have performed six idealized magnetospheric simulations with different model combinations in the SWMF:

[26] 1. Anisotropic MHD Model + RIM
[27] 2. Isotropic MHD Model + RIM
[28] 3. Anisotropic MHD Model + RIM + RCM
[29] 4. Isotropic MHD Model + RIM + RCM
[30] 5. Anisotropic MHD Model + RIM + CRCM
[31] 6. Isotropic MHD Model + RIM + CRCM

[32] The first two simulations do not contain any ring current models, thus they serve as the baselines for comparisons. All six simulations use identical parameters for the same models.

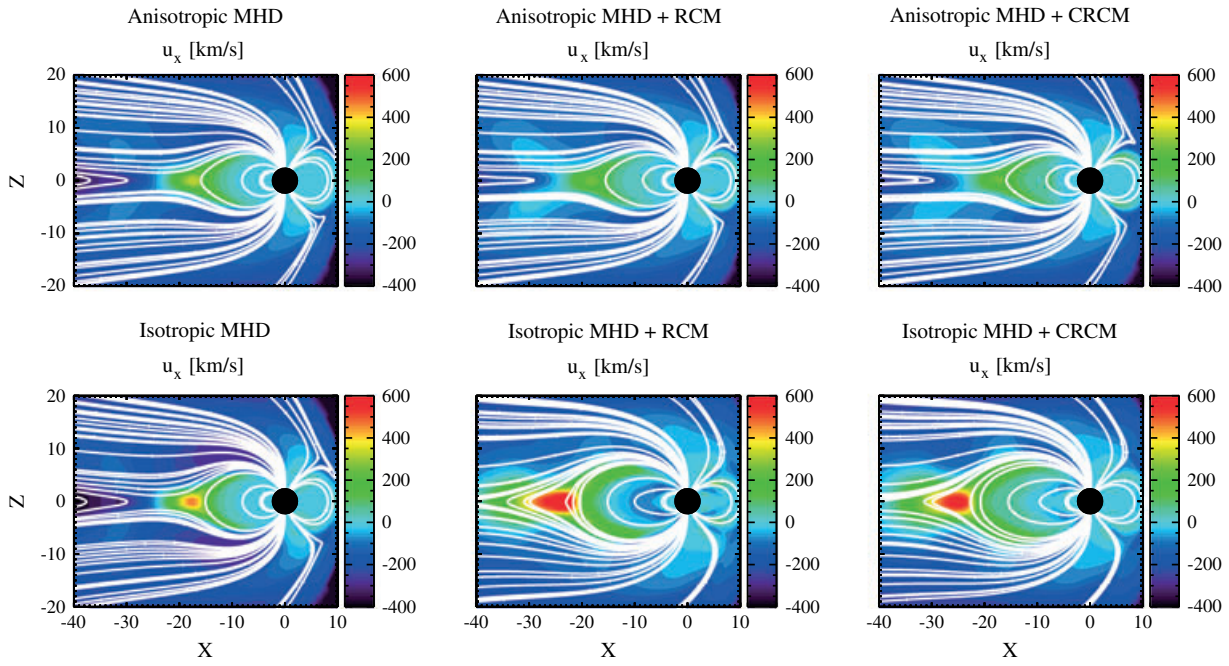

Figure 6. The X direction velocity contour overplotted with the magnetic field lines in the noon-midnight meridional $Y = 0$ plane from the MHD model at $t = 8$ h.

[33] The global MHD model is set up in a 3-D box extended from –224 R_E to 32 R_E in the X direction and from –128 R_E to 128 R_E in the Y and Z directions in the GSM coordinate system. The inner boundary is at 2.5 R_E from the center of the Earth. The grid resolution varies from the smallest 1/8 R_E grid cells close to the Earth to the largest 8 R_E grid cells far down the magnetotail. The total number of cells is 1.8 million. As idealized conditions, we align the magnetic axis with the ecliptic north direction and drive the MHD model with constant solar wind condition and southward IMF: number density n_{sw} = 5 cm^{-3}, temperature T_{sw} = 10^5 K, velocity u_{xsw} = –400 km/s, $u_{y,zsw}$ = 0, magnetic field $B_{x,ysw}$ = 0, and B_{zsw} = –5 nT. We use TVD Lax-Friedrich scheme [*Rusanov*, 1961] with the Koren limiter [*Koren*, 1993], explicit time stepping and Boris factor 0.02, i.e., the reduced speed of light is 6000 km/s.

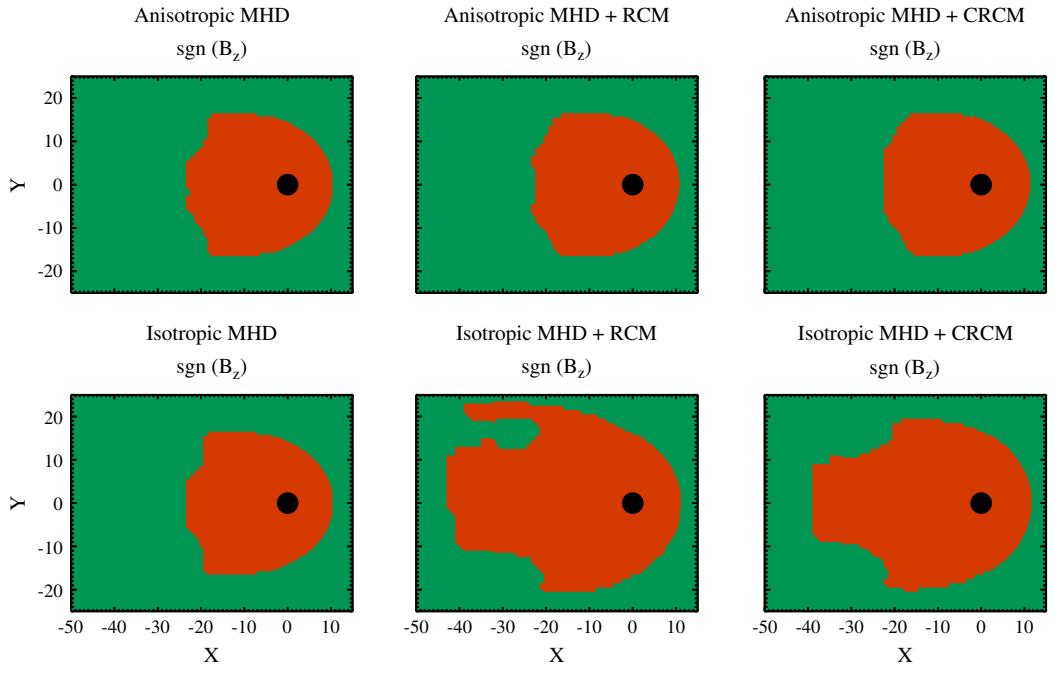

Figure 7. The sign of B_z in the $Z = 0$ plane from the MHD model at $t = 8$ h. Green represents regions with nonpositive B_z, and red represents regions with positive B_z, i.e, closed field line regions.

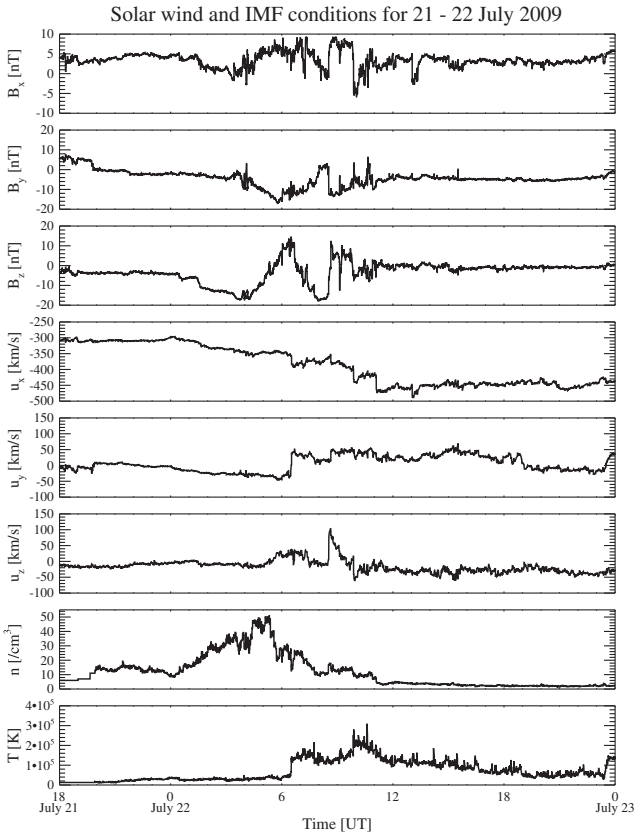

Figure 8. The input solar wind and IMF conditions of the MHD model for the 21–22 July 2009 storm.

[34] For the ionosphere model RIM, we assume a constant Pedersen conductance 5 *mho* and zero Hall conductance. For the RCM, its initial particle distribution is calculated from the MHD solutions of the density and temperature in steady state. For the CRCM, its initial particle distribution is based on quiet time ring current data from the AMPTE/CCE spacecraft [*Sheldon and Hamilton*, 1993].

[35] All simulations are started with 5000 iterations using local time stepping in the MHD model that exchanges information with the RIM every 10 time steps to achieve steady states. Then they are switched to the time accurate mode, and for the last four simulations, are coupled with the RCM or the CRCM. In the time accurate mode, the MHD model is coupled with the RIM every 5 s and with the RCM or the CRCM every 10 s, and the RIM is one-way coupled to the RCM or the CRCM every 5 s. These coupling frequencies are optimal to minimize the computational cost meanwhile ensuring the accuracy of the solutions. The time accurate simulations last for 8 h.

4.1.1. Force Balance Along Closed Field Lines

[36] As mentioned in section 3, the coupling between Anisotropic BATS-R-US and the CRCM is built in a way that the force balance condition along closed field lines is satisfied in the presence of pressure anisotropy. This can be verified by extracting closed field lines in the MHD solution of simulation 5: Anisotropic MHD + RIM + CRCM, and calculate the forces along these field lines based on the force expression (2).

[37] Figure 1 shows examples of the force balance analysis. The top plot displays the logarithmic parallel pressure

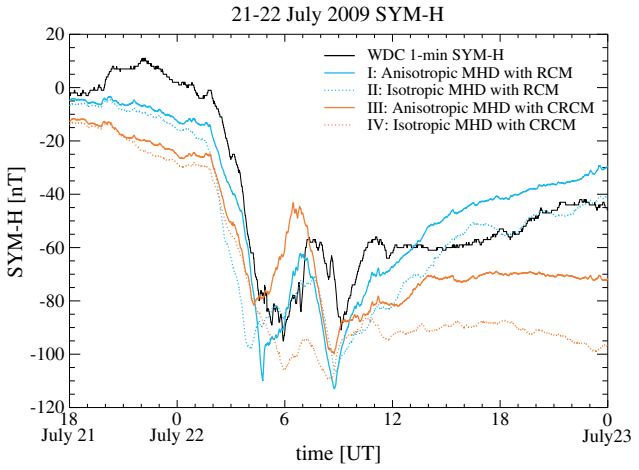

Figure 9. The measured 1 min SYM-H and the simulated SYM-H for the 21–22 July 2009 storm. The blue lines represent the RCM coupled simulations, and the orange ones represent the CRCM coupled simulations. The solid lines are for anisotropic MHD, while the dashed ones are for isotropic MHD.

and the magnetic field lines in the noon-midnight meridional ($Y = 0$) plane at $t = 4$ h from simulation 5. We extract two closed field lines at different locations on the nightside, marked by the black lines. Using the parallel and perpendicular pressures and the magnetic field strength in each grid cell along these two field lines, we calculate the force contributions from the mirror force, i.e., the first term in (2), and from the gradient of the parallel pressure, i.e., the second term in (2). The bottom plots show the forces along these field lines starting from near the inner boundary of the MHD model in the northern hemisphere. In both plots, the mirror force represented by the dotted line and the negative parallel pressure gradient represented by the dashed line are very close to each other. The resulting net force represented by the solid line is approximately zero. The plots demonstrate that the force balance condition is satisfied along the two particular field lines, with some limited discretization errors. Our simulations show no fast field-aligned flows inside the inner magnetosphere, which also confirms the force balance condition.

4.1.2. Pressure Distribution

[38] The plasma pressure distribution in the inner magnetosphere is a direct indication of the ring current. We expect higher inner magnetospheric pressure in the ring current model coupled simulations 3, 4, 5, and 6 compared to the simulations without ring current models. Figure 2 displays the plasma pressure, in the case of anisotropic MHD, the total plasma pressure, from the global MHD model in the equatorial ($Z = 0$) plane at $t = 8$ h. The top three plots are from the three simulations with the anisotropic MHD model,

Table 1. Root-Mean-Square Errors of the Simulated Sym-H for the Two Storms

Time Interval	Run I	Run II	Run III	Run IV
18 UT, 21 Jul–0 UT, 23 Jul	51.3 nT	58.1 nT	62.3 nT	75.6 nT
0 UT–12 UT, 22 Jul 22	37.7 nT	37.3 nT	42.9 nT	57.5 nT
2 UT, 5 Apr–4 UT, 7 Apr	13.9 nT	19.1 nT	14.6 nT	27.0 nT

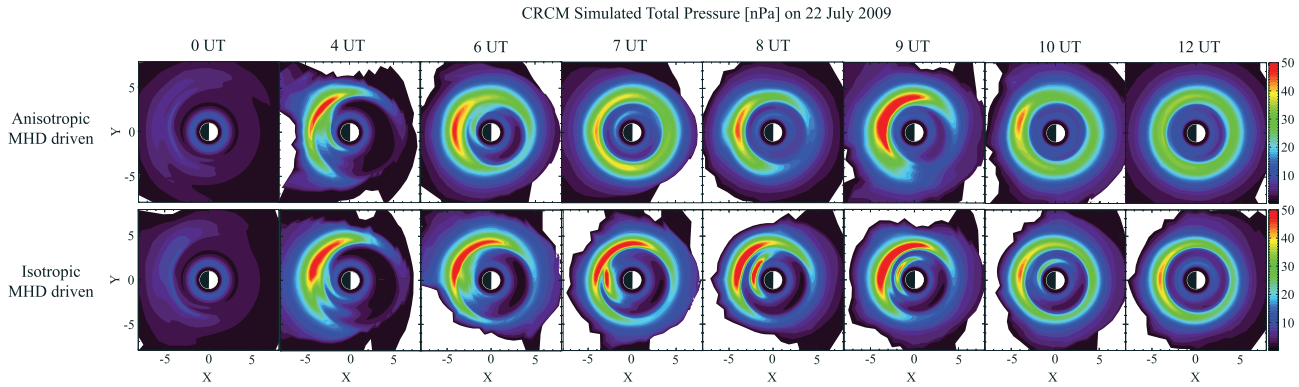

Figure 10. The CRCM simulated total pressure in the $Z = 0$ plane for different times on 22 July 2009. (top) Results from the anisotropic MHD driven case; (bottom) results from the isotropic MHD driven case.

and the bottom ones are from the three simulations with the isotropic MHD model. The comparison among the three top plots shows a much stronger nightside pressure from the RCM or the CRCM coupled anisotropic MHD simulations than from the anisotropic MHD simulation without any ring current model. This validates the effect of the couplings with the RCM and the CRCM, which is consistent with the results from the isotropic MHD simulations shown in the bottom plots. Comparing the anisotropic MHD and isotropic MHD simulation results, we observe higher nightside pressure in the MHD only simulations (Figure 2, left column) and in the CRCM coupled simulations (Figure 2, right column), but lower nightside pressure in the RCM coupled simulations (Figure 2, middle column) for the anisotropic MHD model than for the isotropic MHD model. Comparing the RCM and the CRCM coupled simulations, the latter produces stronger pressure in the anisotropic MHD model but weaker pressure in the isotropic MHD model. Compared to the RCM coupled simulations, the CRCM coupled simulations also show more dawn-dusk asymmetry (dusk preferred) in the pressure distributions, which is caused by the weaker shielding of the inner magnetospheric electric field in the CRCM than in the RCM. Although the RCM and the CRCM coupled simulations react oppositely in terms of changes in the pressure magnitude that resulted from the inclusion of pressure anisotropy in the MHD model, they exhibit similar changes in the size of the inner magnetosphere. When comparing the top and bottom plots in the middle and right columns, we find that the influence of the IM pressure is greatly reduced with anisotropic MHD in comparison with isotropic MHD. We have also noticed that the position of the bow shock varies in these simulations, which will be addressed in section 4.1.3.

[39] A more straightforward comparison of the nightside pressure strengths from different simulations is shown in Figure 3. In this figure we plot the nightside pressure along the Sun-Earth line, i.e., the X axis, from the global MHD model. The solid lines represent anisotropic MHD, and the dotted lines represent isotropic MHD. Compared to the two simulations without ring current models identified by the black lines, we see significant pressure increases in the simulations with the RCM and the CRCM, identified by the blue and orange lines, respectively. The plot clearly shows a little pressure increase in the anisotropic MHD only simulation,

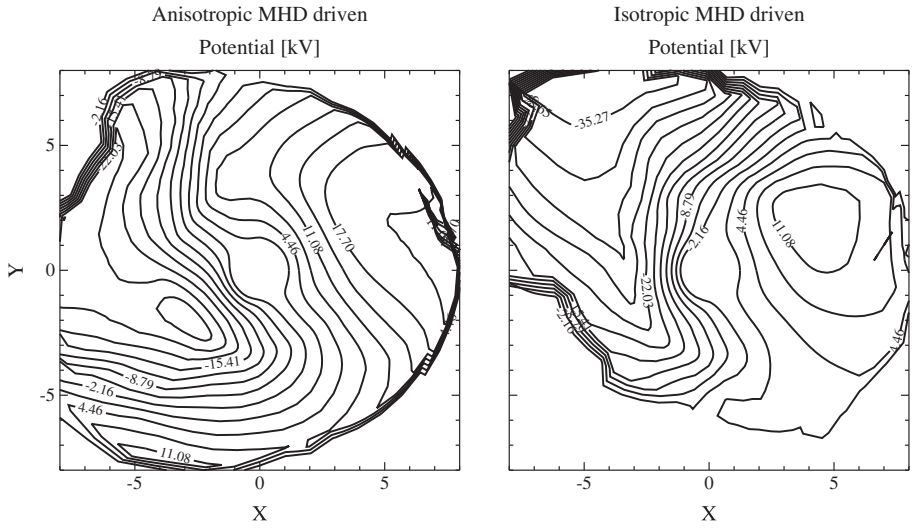

Figure 11. The equatorial electric potential contour from the CRCM at 6 UT on 22 July 2009, mapped along field lines from the solution of the ionospheric electrodynamics model RIM.

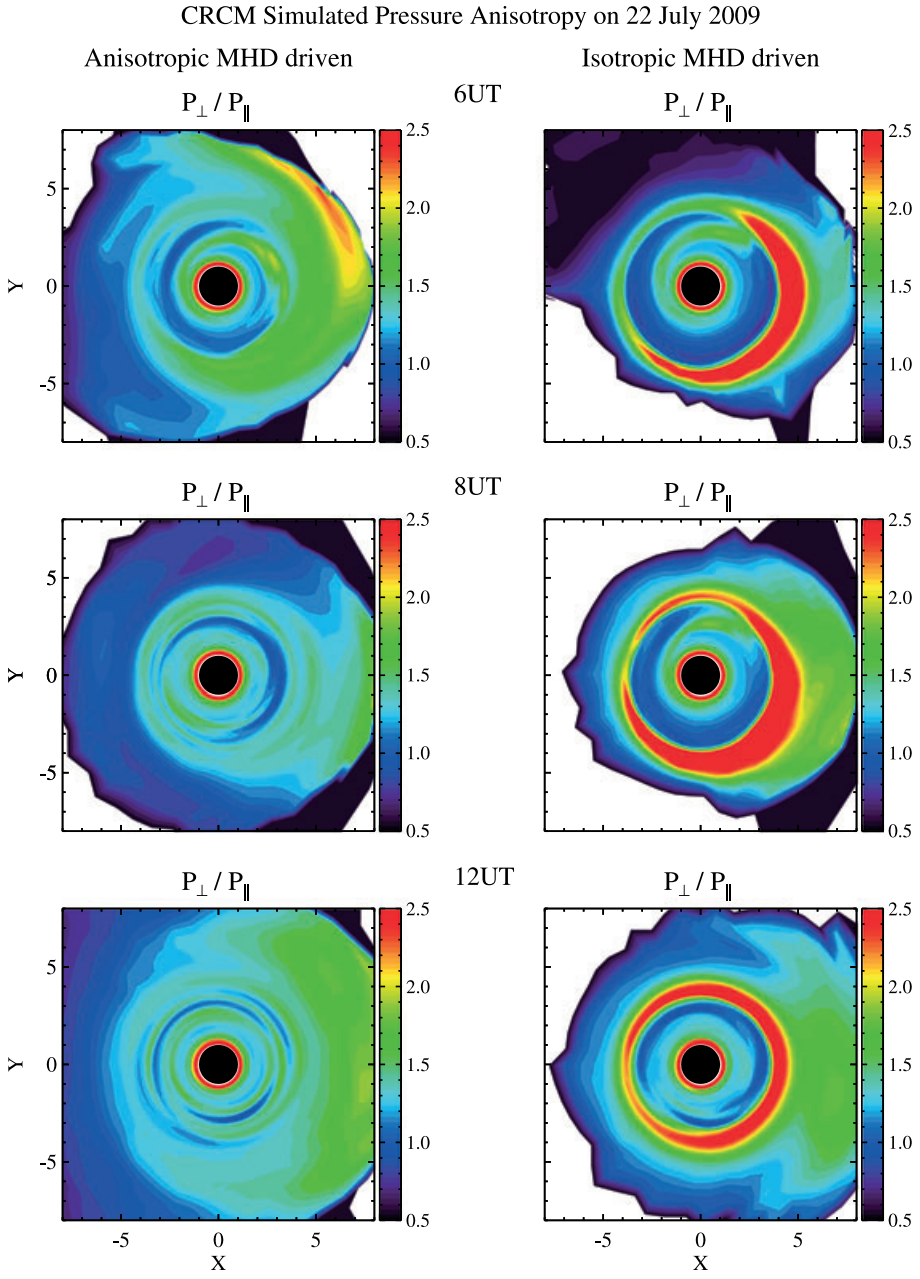

Figure 12. The CRCM simulated pressure anisotropy in the $Z = 0$ plane at (top) 6 UT, (middle) 8 UT, and (bottom) 12 UT on 22 July 2009 for the (left column) anisotropic MHD driven and the (right column) isotropic MHD driven cases.

a large pressure increase in the CRCM coupled anisotropic MHD simulation, but a large pressure decrease in the RCM coupled anisotropic MHD simulation, compared to the corresponding isotropic MHD simulations. Both the RCM and the CRCM coupled anisotropic MHD simulations produce a single pressure peak at around $x = -5\ R_E$. The pressure gradient toward the Earth (which leads to eastward inner ring current), is not very distinctive in the isotropic MHD simulations especially the CRCM coupled one (orange dotted line) in which the pressure gradient toward the Earth is very small.

[40] In the anisotropic MHD simulations we can also look into pressure anisotropy. Figure 4 shows the pressure anisotropy ratio $P_\perp/P_\parallel$ in the $Z = 0$ plane at $t = 8$ h from the MHD model. In the inner magnetosphere region within 8 R_E radius, the RCM coupled simulation has the least amount of pressure anisotropy with an exception of a parallel pressure dominated small region close to the Earth, while the CRCM coupled simulation has the strongest pressure anisotropy with the perpendicular pressure dominating in general. This is expected, since the coupling with the isotropic RCM drives the pressure toward isotropy in the closed field line region. Therefore, the RCM coupled simulation produces less pressure anisotropy than the anisotropic MHD only simulation does. The CRCM coupled simulation, on the other hand, produces more pressure anisotropy than the anisotropic MHD only simulation does, behind the magnetosheath particularly, which implies that the CRCM itself

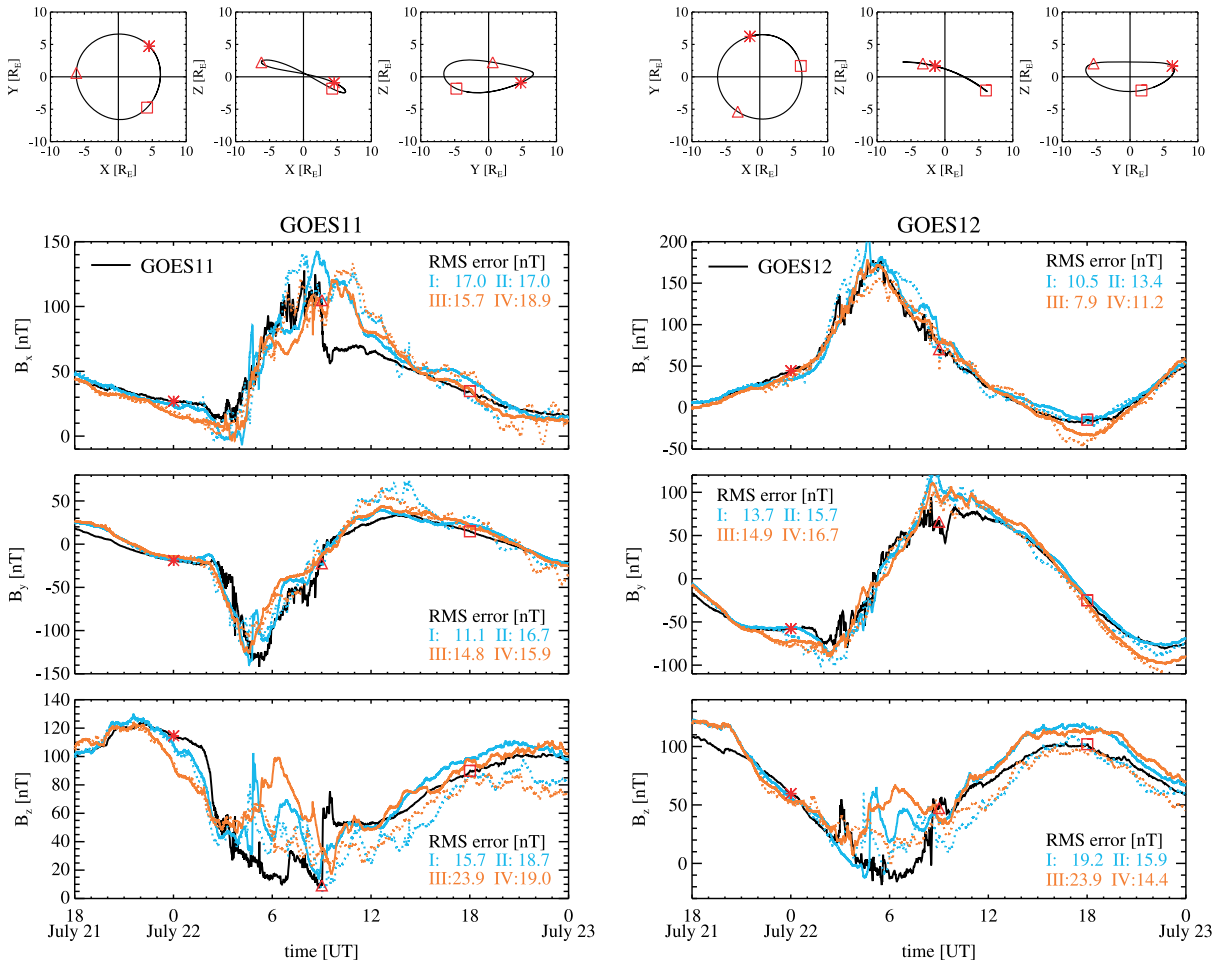

Figure 13. The orbits of (top left) GOES11 and (top right) GOES12 from 18 UT on 21 July to 0 UT on 23 July and the measured and simulated magnetic field with the root-mean-square (RMS) errors written on the plots. The line representations of the four simulations are the same as in Figure 9.

generates more perpendicular preferred pressure anisotropy than the anisotropic MHD model does.

4.1.3. Magnetosheath Thickness and Magnetopause Position

[41] In the previous study [*Meng et al.*, 2012a], we have found thicker magnetosheath when including pressure anisotropy in global MHD simulations. However, this changes for simulations coupled with the RCM or the CRCM. Figure 5 plots the number density, pressure (total pressure in the anisotropic MHD cases) and magnetic field strength variations along the Sun-Earth line on the dayside from the MHD solutions at t = 8 h. For the two MHD only simulations represented by the black lines, we see a larger bow shock stand-off distance from the Earth and a wider magnetosheath in the case of anisotropic MHD. In addition, the position of the magnetopause is not affected much by pressure anisotropy. On the contrary, for the RCM and the CRCM coupled simulations, pressure anisotropy brings both the magnetopause and the bow shock closer to the Earth, resulting in a thinner magnetosheath as the change of the bow shock stand-off distance is larger than the change of the magnetopause position, which can be seen from the number density and pressure profiles. The thickness of the magnetosheath from different simulations can be ordered from the thinnest to the thickest as follows: Isotropic MHD, Anisotropic MHD + CRCM, Anisotropic MHD, Anisotropic MHD + RCM, Isotropic MHD + CRCM, Isotropic MHD + RCM. The different effects of pressure anisotropy on the thickness of magnetosheath in MHD only and RCM or CRCM coupled simulations are likely due to the combined results from both the bow shock jump relations and the position of the magnetopause. *Spreiter et al.* [1966] has found that the width of the magnetosheath (Δ) is proportional to the ratio of the densities in the solar wind (ρ_{sw}) and behind the bow shock (ρ), and is proportional to the stand-off distance of the magnetopause from the center of the Earth (D), i.e., $\Delta \propto D\rho_{sw}/\rho$. For the two MHD only runs, with the almost identical magnetopause locations, anisotropic MHD gives a smaller density jump across the bow shock than isotropic MHD, which leads to a thicker magnetosheath in the anisotropic MHD case as its magnetosheath plasma is less dense. For the RCM and CRCM coupled runs, the anisotropic MHD cases have smaller density jumps but closer magnetopauses to the Earth, which result in thinner magnetosheaths than the isotropic MHD cases. This implies that the magnetopause position is a more important factor in determining the magnetosheath thickness in these particular simulations.

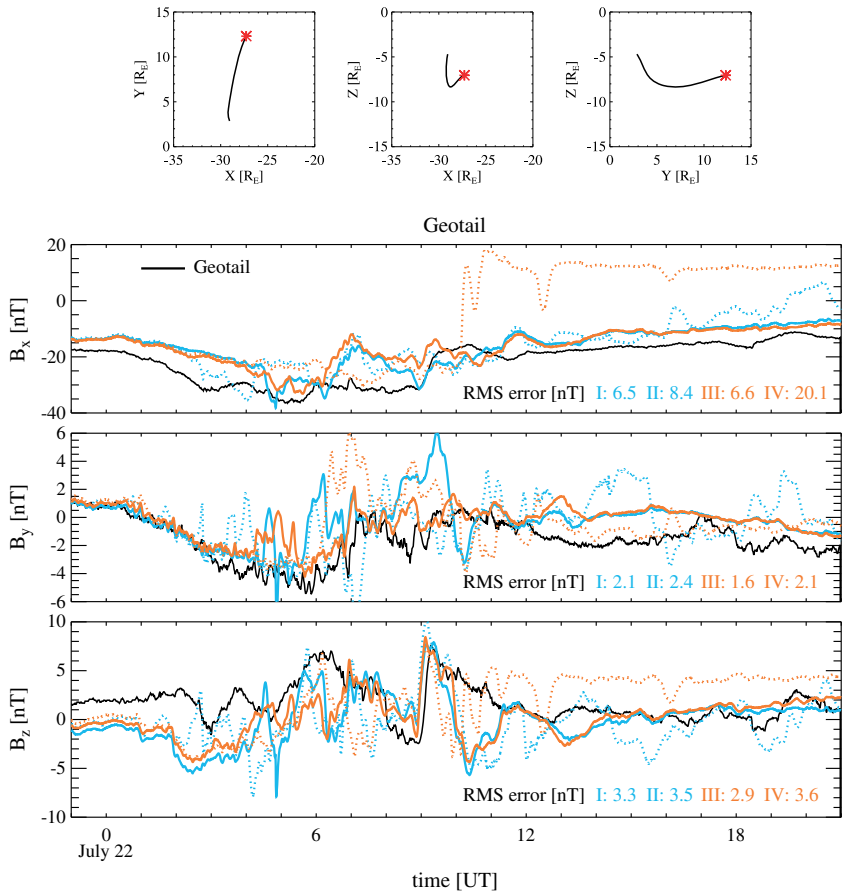

Figure 14. (top) The orbits of Geotail from 18UT on 21 July to 0UT on 23 July and the measured and simulated magnetic field with the root-mean-square errors. The line representations of the four simulations are the same as in Figure 9.

[42] The magnetopause positions from the RCM and the CRCM coupled simulations are further away from the Earth compared to the ones in MHD only simulations. This could be easily explained by the larger inner magnetospheric pressure in the ring current model coupled simulations, which blows up the size of the whole magnetosphere. The closer magnetopause from the Earth in the RCM and the CRCM coupled simulations in the anisotropic MHD case than in the isotropic MHD case is consistent with the pressure distribution plots in the middle and right columns of Figure 2, which shows a reduced pressure just inside the magnetopause and thus a smaller magnetosphere in the anisotropic MHD case.

4.1.4. Earthward Tail Flow and Magnetic Field Configuration

[43] Another conclusion from the previous study is that the inclusion of pressure anisotropy in the global MHD model reduces the reconnection rate thus the Earthward flow speed in the tail. This holds true for the ring current model coupled MHD simulations, too. Figure 6 displays the X direction flow speed as well as the magnetic field lines in the $Y = 0$ plane from the MHD solutions at $t = 8$ h. The comparison between the top and bottom plots in each column shows greatly reduced Earthward flow speeds in the cases of anisotropic MHD compared to isotropic MHD. For the RCM and the CRCM coupled simulations (Figures 6, middle and 6, right columns), this flow speed reduction is more significant than the MHD only simulations (Figure 6, left column). For anisotropic MHD (Figure 6, top row), the Earthward flow in the RCM or the CRCM coupled case is even slower than the one in the MHD only case.

[44] Figure 6 also shows the change in the shape of the magnetic field lines when including pressure anisotropy in the MHD model coupled with the RCM or the CRCM. In the anisotropic MHD only simulation, the magnetic field configuration is barely different from the one in the isotropic MHD only simulation. However, with the coupling of the ring current models, the tail reconnection site in anisotropic MHD is much closer to the Earth than in isotropic MHD, and the overall shape of the closed field lines is compressed in anisotropic MHD. This, again, is consistent with the reduced size of the inner magnetosphere in anisotropic MHD that we discussed previously. An interesting feature of the three bottom plots is that the coupling of the ring current models changes the magnetic field configuration significantly in the isotropic MHD case. But this effect is almost eliminated in the anisotropic MHD case, for which the coupling of the ring current models does not seem to impact the magnetic field configuration, at least not distinguishable in the plots. A better view is shown in Figure 7, which displays the sign of the B_z component in the equatorial plane for the six cases. The red-colored region in each plot essentially represents the closed field line region in the corresponding

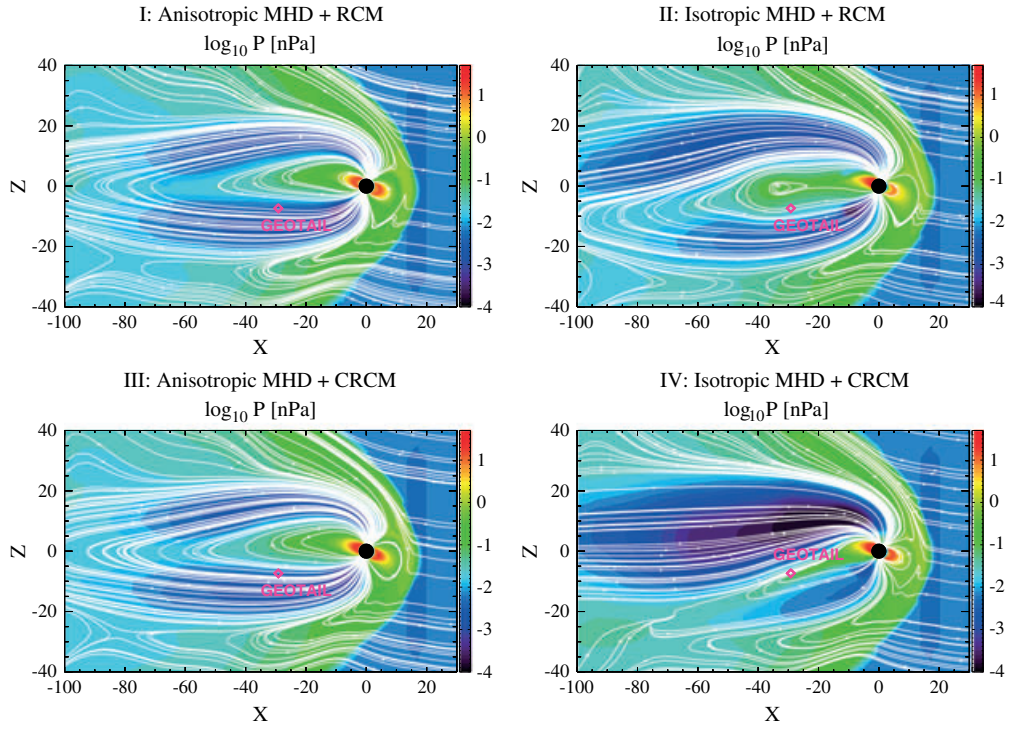

Figure 15. The logarithm of the total pressure and the magnetic field lines in the $Y = 0$ plane at 12UT on 22 July from the MHD solutions.

simulation. The figure indicates that pressure anisotropy completely eliminates the field line configuration change due to the coupling with the RCM or the CRCM. This implies the importance of pressure anisotropy in controlling magnetic field configuration. Even though the pressure anisotropy in the global MHD model might be small in the inner magnetosphere, for instance, in the anisotropic MHD + RCM simulation, it still has a strong effect on the closed magnetic field region.

4.2. Geomagnetic Storms

[45] Geomagnetic storm simulations require incorporating a kinetic inner magnetosphere model with the global MHD model in order to capture the dynamics of the ring current during storm evolutions, thus can be used to validate the coupling between the anisotropic MHD model and the RCM or the CRCM.

[46] We set up the storm simulations the same way as we do the idealized magnetospheric simulations, except that real physical parameters replace the idealized conditions. For the global MHD model, we set orientations of the magnetic and the rotational axes based on the actual time and date to be simulated. The input time-varying solar wind and IMF conditions are taken from the ACE and/or WIND measured values that are time-shifted based on the solar wind propagation time from the satellite to the upstream boundary of the simulation. For the RIM, we use the actual solar $F10.7$ flux to calculate the ionospheric conductance. For the RCM, we use a 10 h artificial decay term to mimic the SYM-H recovery. This artificial term is not added to the CRCM as several loss mechanisms for ring current particles are incorporated in that model.

[47] In this study we simulate two moderate storm events, one in 2009 and the other in 2010. For each event, we conduct four simulations:

[48] Run I: Anisotropic MHD Model + RIM + RCM

[49] Run II: Isotropic MHD Model + RIM + RCM

[50] Run III: Anisotropic MHD Model + RIM + CRCM

[51] Run IV: Isotropic MHD Model + RIM + CRCM

4.2.1. The 21–22 July 2009 Storm

[52] The first event we select is the 21–22 July 2009 CIR-driven storm. The time interval we simulate is from 18 UT on 21 July to 0 UT on 23 July. The upstream condition input for the global MHD model is shown in Figure 8. The IMF z component slowly decreases, accompanied by a density increase starting at 0 UT, 22 July, which triggers the storm. Later B_z changes from southward to northward, then southward, then northward again, which continues to disturb the magnetosphere.

[53] The SYM-H index reflects the variation of ring current strength during the storm. Figure 9 compares the simulated SYM-H indexes by the global MHD model from different simulations and the measured 1 min SYM-H index. For the RCM coupled simulations represented by the blue lines, we see differences in the storm main phase and the recovery phase between the anisotropic MHD simulation and the isotropic MHD simulation. The anisotropic MHD simulation has a slightly deeper SYM-H decrease between 0 UT and 4 UT of the main phase, which matches the data better. The same conclusion can be drawn for the recovery phase between 10 UT and 14 UT. During other times, the anisotropic MHD simulation predicts worse SYM-H than the isotropic MHD simulation. For the CRCM coupled simulations, the anisotropic MHD and the isotropic MHD make a big difference in the main phase, with the

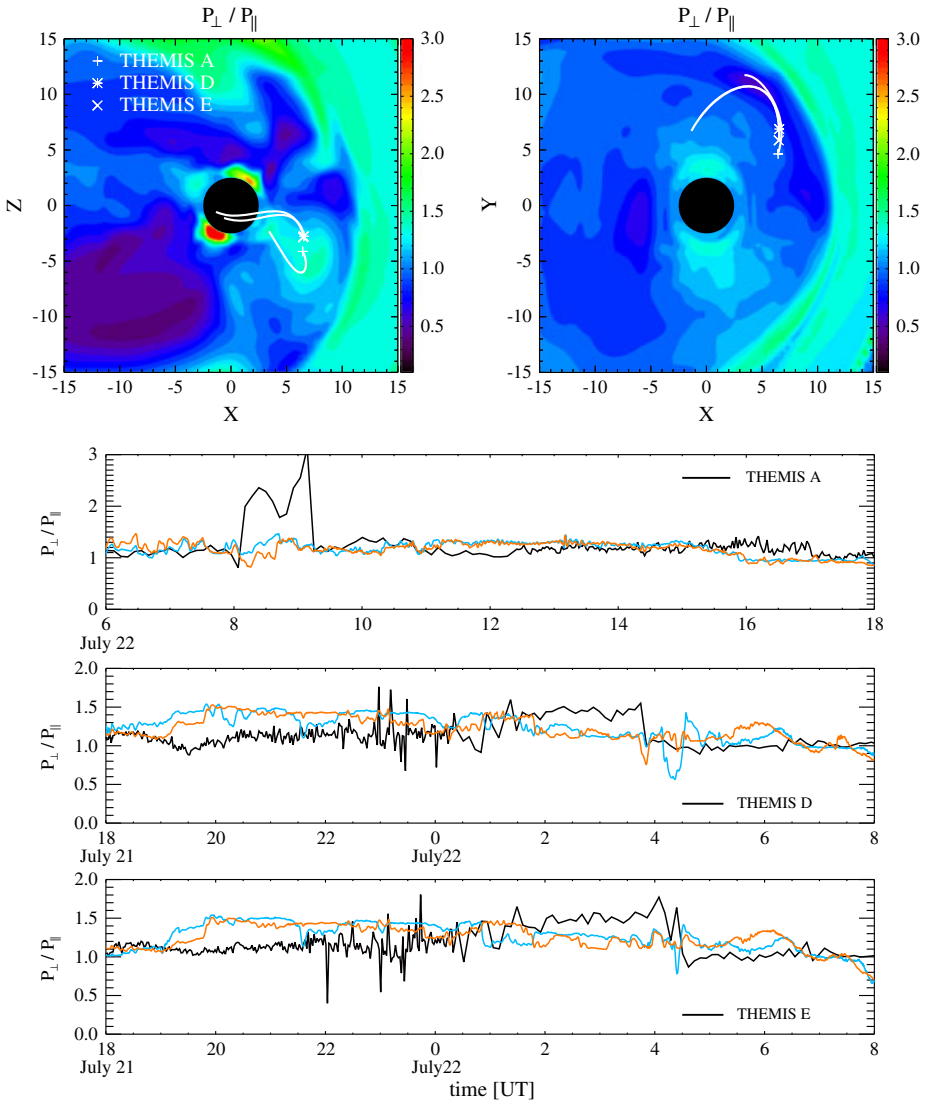

Figure 16. The pressure anisotropy in the (top left) $Y = 0$ and (top right) $Z = 0$ planes at 16 UT on 22 July, overplotted with the orbits of THEMIS A, D, and E (white lines) during the 21–22 July 2009 storm. The lower three panels show the measured and simulated pressure anisotropy. The blue line represents the RCM coupled anisotropic MHD simulation, and the orange line represents the CRCM coupled anisotropic MHD simulation.

anisotropic MHD predicting much less SYM-H. In the recovery phase, the SYM-H of the anisotropic MHD case recovers faster than the SYM-H of the isotropic MHD case. For a better comparison, Table 1 provides the root-mean-square errors during the entire simulated interval and the main phase (0 UT to 12 UT, 22 July), which indicates that in terms of the root-mean-square error of SYM-H, the anisotropic MHD simulations are consistently better than the isotropic MHD simulations, except during the main phase of the RCM coupled simulations when the anisotropic MHD case is slightly worse. From Figure 9, we have also noticed that the SYM-H recovers much slower in the CRCM coupled simulations than it does in the RCM coupled simulations. On one hand, we have applied the artificial decay term for the RCM coupled simulations. On the other hand, the CRCM underestimates the decay rate of the ring current.

4.2.1.1. CRCM Solutions

[54] Since the coupling between Anisotropic BATS-R-US and the CRCM provides the first opportunity for the CRCM to be driven by an anisotropic MHD model self-consistently, we are also interested in the differences in the CRCM solutions when driven by the anisotropic MHD model compared to the solutions when driven by the isotropic MHD model.

[55] Figure 10 displays the total pressure in the equatorial plane from the CRCM in simulations III and IV. A series of plots at different times during the storm is shown, which represents the evolution of the ring current. The anisotropic MHD driven case (Figure 10, top) and the isotropic MHD driven case (Figure 10, bottom) generate very different ring current patterns at same times. At 0 UT just before the storm begins, the anisotropic MHD driven case gives very similar, though very weak, pressure distribution as the isotropic MHD driven case does. At 4 UT when the storm grows, the

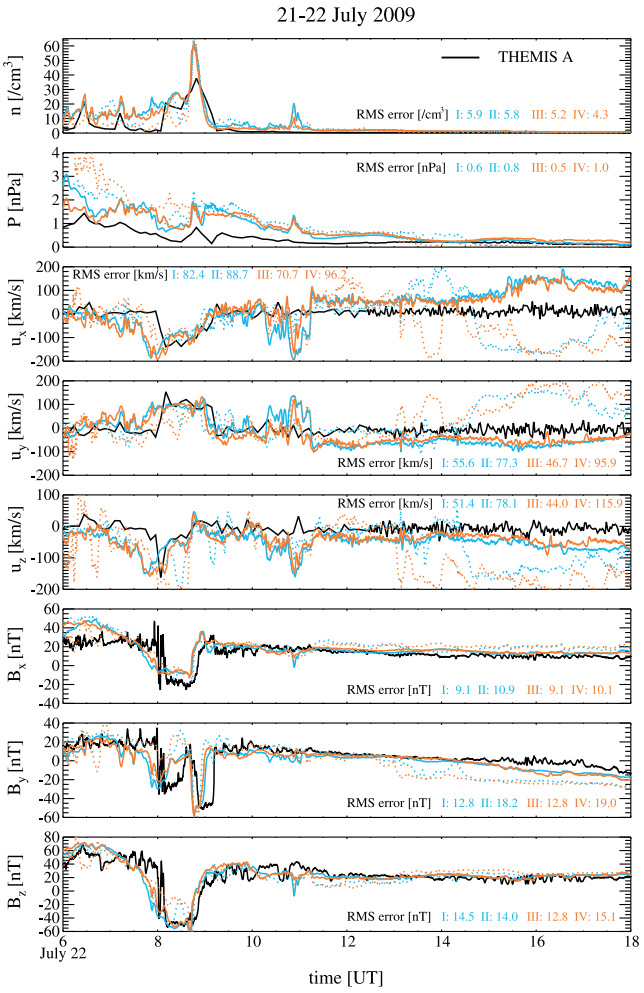

Figure 17. The simulated density, pressure, velocity, and magnetic field along the THEMIS A trajectory from the MHD solutions and the actual measurement for the 21–22 July 2009 storm. The line representations of the four simulations are the same as in Figure 9.

anisotropic MHD driven case has a weaker ring current than the isotropic MHD driven case has, but in both cases the ring current has a strong duskside preference. From 6 UT to 8 UT during the storm main phase, the anisotropic MHD driven case shows a much weaker and more dawn-dusk symmetric ring current than the other simulation. Moreover, the ring current undergoes a strong-weak-strong change from 6 UT to 8 UT in the anisotropic MHD driven case, which is due to the southward-northward-southward IMF turning during this time shown in Figure 8, yet this variation is not distinctive in the isotropic MHD driven case. This difference can also be seen from the SYM-H variations in Figure 9. Between 6 UT and 8 UT, the SYM-H index in simulation III increases then decreases, while the SYM-H in simulation IV has a much smaller change. The consistency between the results from the global MHD model and from the CRCM also verifies the correct coupling between these models. After 9 UT, the start of the recovery, the ring current patterns in the anisotropic MHD and isotropic MHD driven cases become closer. However, the anisotropic MHD case shows a faster ring current decay, so that at 12 UT, the pressure is obviously less and its distribution is more symmetric surrounding the Earth. An overview of the ring current strengths at all times in Figure 10 tells us that the CRCM produces weaker ring current when driven by the anisotropic MHD model than by the isotropic MHD model for this storm.

[56] As a further exploration, we plot the equatorial electric potential contours from the CRCM at 6 UT for both the anisotropic MHD and isotropic MHD driven simulations in Figure 11. The potential distribution in the equatorial plane is traced along the closed field lines from the potential pattern in the high latitude ionosphere solved by the RIM. This potential is due to the convection electric field, thus the equipotential lines represent drift paths of zero (or very low) energy particles. For high energy particles, their motions are also governed by the azimuthal gradient-curvature drift that is energy dependent. In the anisotropic MHD driven case shown in Figure 11, left, the equipotential lines are more tilted eastward near dawn compared to the isotropic MHD driven case shown in the Figure 11, right. The tilted equipotential lines extend across the nightside toward dusk. This causes more ions injected from the nightside to be on open drift paths and lost at the dusk boundary in the anisotropic MHD driven case than in the isotropic MHD driven case. As a result, the overall ion pressure is lower in the former case. For the isotropic MHD driven case, the equipotential

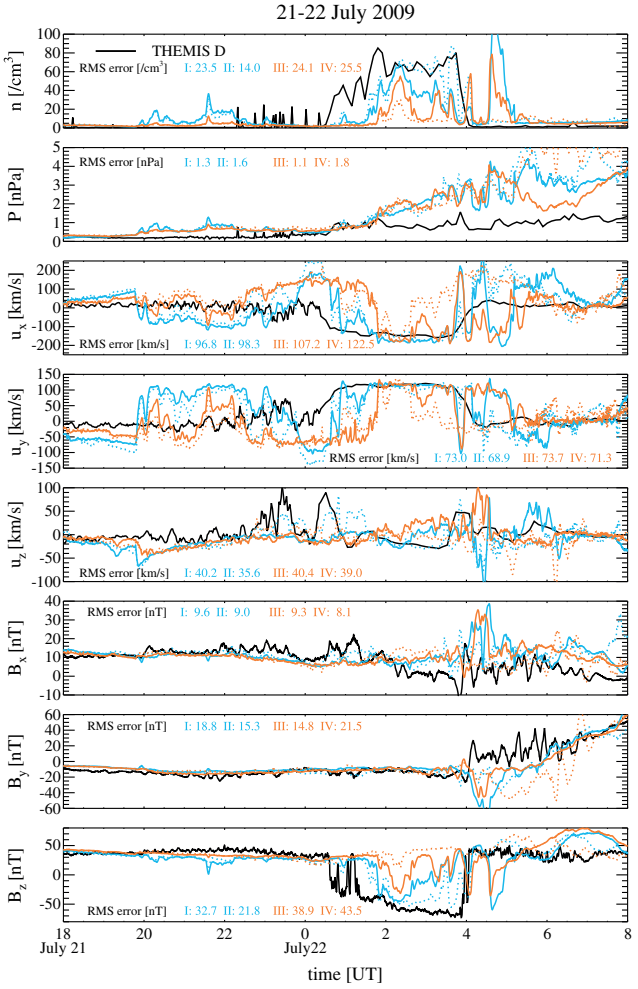

Figure 18. Same as Figure 17, but for THEMIS D.

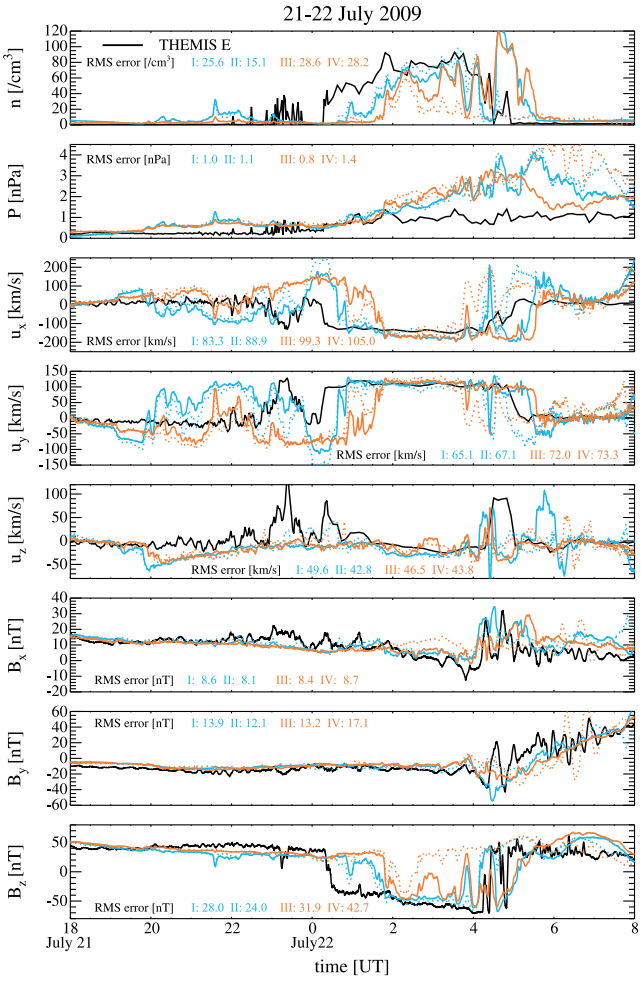

Figure 19. Same as Figure 19, but for THEMIS E.

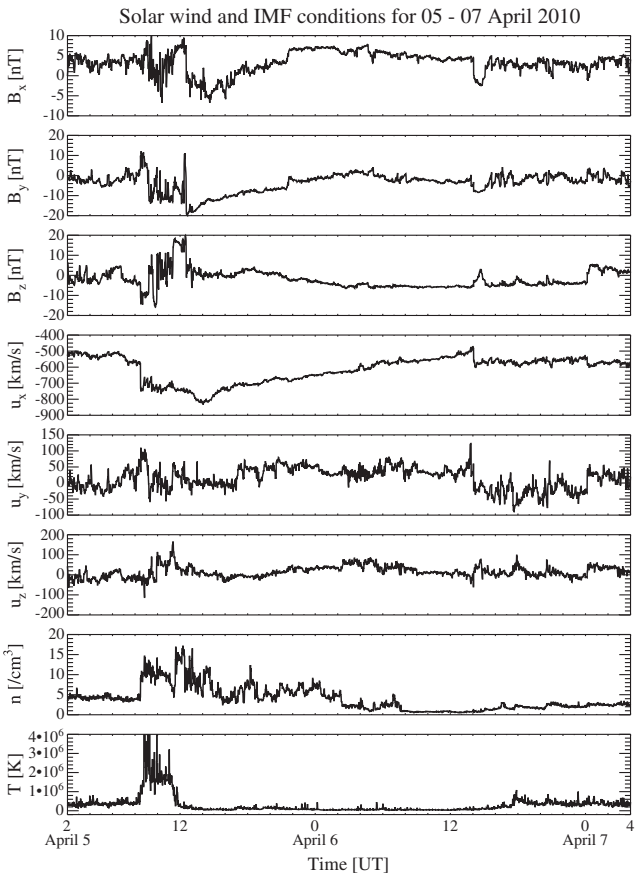

Figure 20. The input solar wind and IMF conditions of the MHD model for the 5–7 April 2010 storm.

lines are bent westward by strong field-aligned currents on the duskside. Together with the gradient-curvature drift, ions drift westward to the dayside through dusk, creating a strong dawn-dusk asymmetry in pressure.

[57] Including pressure anisotropy in the global MHD model also modifies the pressure anisotropy in the CRCM for the coupled simulations. Figure 12 plots the pressure anisotropy in the $Z = 0$ plane in the CRCM at three different times. Figure 12 (left column) shows the anisotropic MHD driven case, and Figure 12 (right column) shows the isotropic MHD driven case. Overall, the anisotropic MHD driven CRCM produces much less pressure anisotropy than the isotropic MHD driven CRCM does. This results from the deeper penetration of the particles in the isotropic MHD driven case, which leads to more perpendicular pitch angle distribution due to the strong gradient-curvature drift and charge exchange loss that prefer to remove particles moving along the field lines. In the more self-consistent simulation (anisotropic MHD with the CRCM), we observe pressure anisotropy variation during the storm. At 6 UT when the storm enters the main phase, the pressure is highly perpendicular especially on the dayside. At a later time 8 UT, the anisotropy becomes less. At 12 UT during the recovery phase, the pressure anisotropy increases, and the region with perpendicular preferred pressure grows larger.

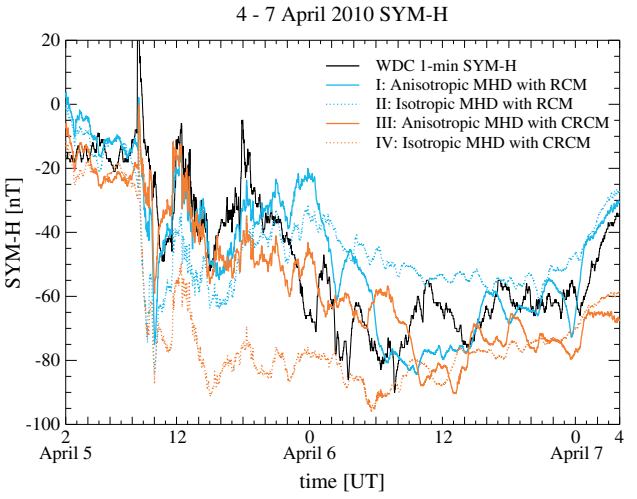

Figure 21. The measured 1 min SYM-H and the simulated SYM-H for the 5–7 April 2010 storm. The blue lines represent the RCM coupled simulations, and the orange ones represent the CRCM coupled simulations. The solid lines are for anisotropic MHD, while the dashed ones are for isotropic MHD.

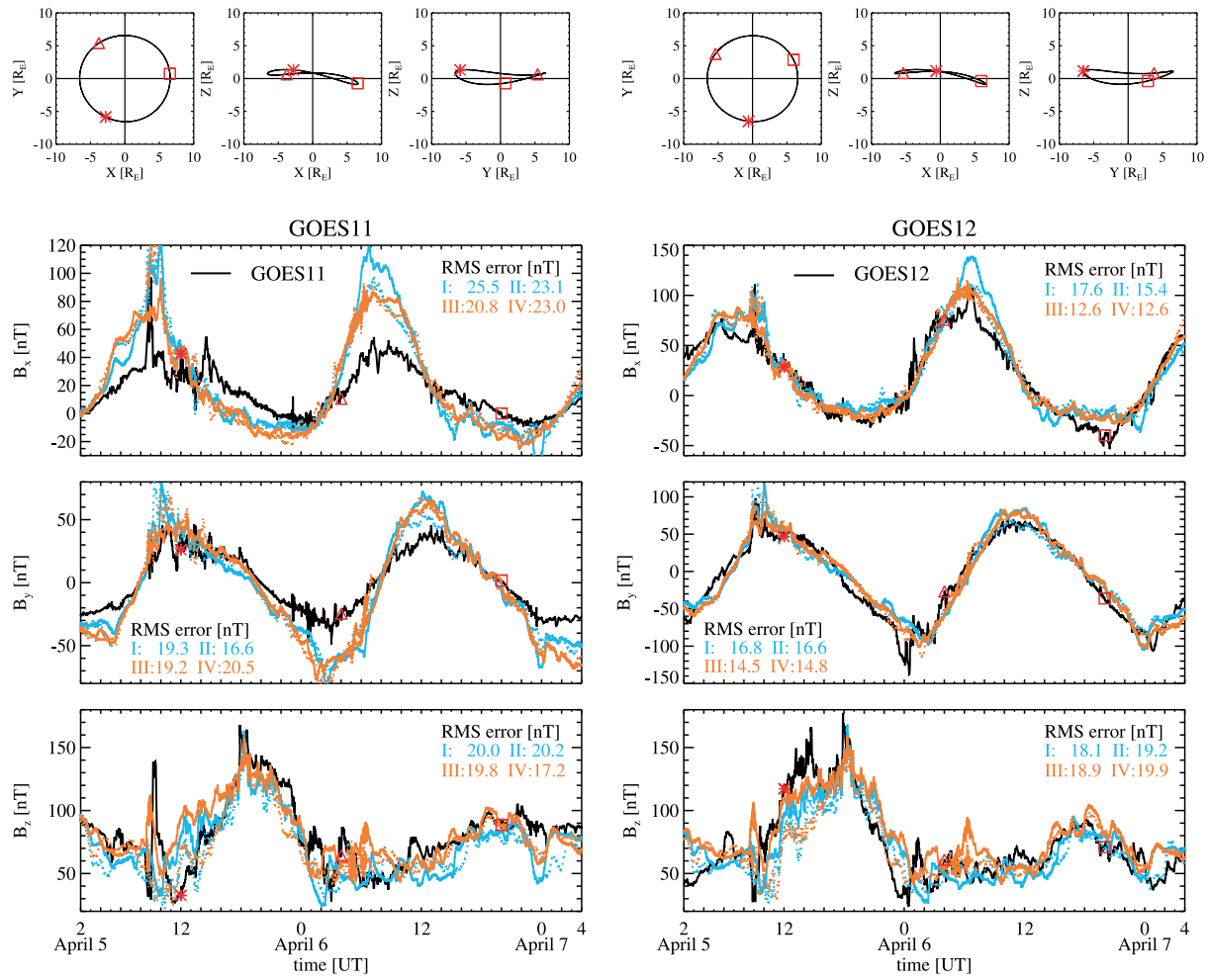

Figure 22. The orbits of (top left) GOES11 and (top right) GOES12 from 2 UT on 5 April to 4 UT on 7 April and the measured and simulated magnetic field with the root-mean-square errors written on the plots. The line representations of the four simulations are the same as in Figure 21.

4.2.1.2. Comparison With Satellite Data

[58] We trace a number of satellites in the global MHD model and extract the variables along the satellite trajectories for the four simulations. The simulated results are compared to the actual data.

[59] Figure 13 shows the GOES11 and GOES12 orbits during the storm and the comparison between the simulated and measured magnetic field along the geosynchronous orbit. We use the same line types and colors to distinguish different simulations as those we use in Figure 9. We calculate the root-mean-square errors for quantitative comparisons, also shown in the figure. For both the RCM coupled and the CRCM coupled simulations, the anisotropic MHD model matches the measured X and Y components of the magnetic field better, but does worse for the Z component, than the isotropic MHD model does. In terms of the shape of the magnetic field lines, the anisotropic MHD model predicts less stretched magnetic field lines than the isotropic MHD model does during the main phase and the recovery phase of the storm. For the anisotropic MHD case, the RCM coupled and the CRCM coupled simulations are competitive in terms of reproducing the magnetic field.

[60] The comparison with the Geotail data indicates significant improvements when using theanisotropic MHD model instead of the isotropic MHD model for ring current coupled simulations, as shown in Figure 14. During this storm time interval, Geotail was down in the tail at about $X = -30\ R_E$. For both the RCM and the CRCM coupled cases, the anisotropic MHD model produces better agreement with data for all three components of the magnetic field than the isotropic MHD model does. Moreover, the CRCM coupled anisotropic MHD simulation matches the measured magnetic field in the tail best among the four simulations. We have also noticed that the CRCM coupled isotropic MHD simulation predicts B_x with the wrong sign from 10UT, 22 July to 0UT, 23 July. To further investigate this problem, we look into the simulated magnetic field configuration at 12UT on 22 July when simulation IV has a very different B_x from the other simulations and the data, shown in Figure 15. We overplot the field lines on the logarithmic pressure contour in the $Y = 0$ plane, as well as the Geotail location at 12UT projected to this plane, represented by the magenta diamond. In simulation IV, the tail is very tilted toward the minus Z direction, so that Geotail is on the opposite side of the current sheet to where it is in the other three simulations.

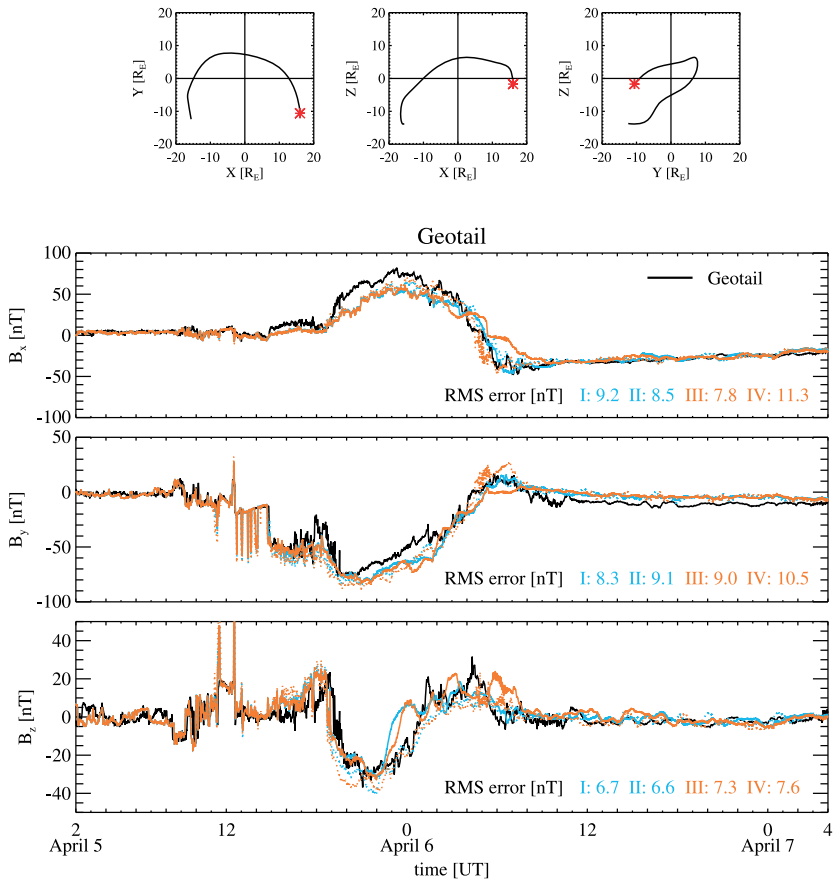

Figure 23. The orbits of (top) Geotail from 2 UT on 5 April 5 to 4 UT on 7 April and the measured and simulated magnetic field with the root-mean-square errors. The line representations of the four simulations are the same as in Figure 21.

Hence, the simulated B_x is positive instead of negative in simulation IV.

[61] During the July 2009 storm, the THEMIS data is also available. Since THEMIS satellites measure the perpendicular and parallel temperatures, we could compare the simulated pressure anisotropy to the measurement directly. Figure 16 shows the orbits of THEMIS A, D, and E projected in the $Y = 0$ and $Z = 0$ planes with the simulated pressure anisotropy from simulation III at 16UT on 22 July, and the simulated pressure anisotropy ratio extracted along the satellite trajectories compared with the actual data. All three satellites are in the dusk sector of the dayside magnetosphere. THEMIS D and E have very close trajectories. The pressure anisotropy contour plots show that perpendicular pressure dominates the polar regions, the magnetosheath, and the region close to the Earth. The simulated $P_\perp/P_\parallel$ matches the data reasonably for both the RCM and the CRCM coupled simulations except the pressure anisotropy jump between 8 UT and 9 UT seen by THEMIS A. Later we will see that during this time interval, THEMIS A went across the magnetopause and into the magnetosheath where the pressure anisotropy is high.

[62] We also compare the other variables measured by the THEMIS satellites with the simulated ones. Figures 17–19 display the data-model comparisons of the number density, pressure, velocity, and magnetic field for THEMIS A, D, and E, respectively. For THEMIS A, both the RCM and the CRCM coupled anisotropic MHD simulations (I and III) improve the comparisons for almost every variable, especially for the velocity, relative to the isotropic MHD simulations (II and IV). In the velocity comparison, the isotropic MHD simulations predict large flows after 13UT, which are not observed. The RCM and the CRCM coupled anisotropic MHD simulations are very competitive with each other in terms of matching the actual data. At 8UT, B_z has a sudden decrease and the number density has a sudden increase, which implies that the satellite flew into the magnetosheath. Although the simulations capture the change in the magnetic field, they miss the anisotropy jump. For THEMIS D and E, the anisotropic MHD simulations do not show improvements as large as they are for THEMIS A. For the RCM coupled simulations, anisotropic MHD produces even worse results than isotropic MHD does for some variables, for example, the number density. For the CRCM coupled simulations, the anisotropic MHD model still has better results than the isotropic MHD model has for most variables. Interestingly, for these satellite trajectories, the RCM coupled isotropic MHD simulation II seems to do a better job than the CRCM coupled anisotropic MHD simulation III.

4.2.2. The 5–7 April 2010 Storm

[63] The second event we select is the 5–7 April 2010 CME-driven storm. The simulated time interval is from 2 UT on 5 April to 4 UT on 7 April. The input solar wind and IMF conditions are from the ACE satellite measurement,

shown in Figure 20. The CME arrives shortly after 8 UT, when the IMF B_z starts to decrease, the solar wind speed suddenly increases, and the number density and temperature suddenly increase.

[64] Figure 21 shows the simulated and measured SYM-H index, from which we could tell that the anisotropic MHD simulations predict better SYM-H for this storm than the isotropic MHD simulations do, also shown by the root-mean-square errors for the simulated time interval in the last row of Table 1. In particular, for the CRCM coupled simulations, the anisotropic MHD case produces much closer SYM-H to the measurement than the isotropic MHD case does. The CRCM coupled isotropic MHD simulation produces overly large negative SYM-H, which indicates that it overestimates the ring current strength. The two anisotropic MHD simulations are competitive, with the RCM coupled simulation matching the measured SYM-H after 12 UT on 6 April better than the CRCM coupled one, but the SYM-H recovery simulated by the RCM coupled simulation could have mostly resulted from the artificial decay term we added.

[65] Comparisons of the simulated magnetic field at the geosynchronous orbit to the GOES satellite measurement are presented in Figure 22. In general, for the CRCM coupled simulations, the anisotropic MHD model captures the variations in the data better than the isotropic MHD model does. On the contrary, for the RCM coupled simulations, the anisotropic MHD model does slightly worse. Of the two anisotropic MHD simulations, the CRCM coupled one does better than the RCM coupled one particularly for B_x. However, all simulations produce less stretched field lines than as seen by GOES11.

[66] The comparison with the Geotail data is shown in Figure 23. During the storm, Geotail moved from outside the bow shock to the inner magnetosphere. All four simulations reproduce the measured magnetic field well. Between the two CRCM coupled simulations, the anisotropic MHD simulation matches the data better according to the root-mean-square errors. The CRCM coupled anisotropic MHD simulation and the two RCM coupled simulations are competitive.

5. Conclusions

[67] In order to address the ring current dynamics during the geomagnetic disturbed time with our newly developed anisotropic MHD model, we couple Anisotropic BATS-R-US with the RCM and the CRCM. Since the CRCM can resolve pitch angle anisotropy while the RCM cannot, the coupling between Anisotropic BATS-R-US and the CRCM is more self-consistent. For the first time, we provide two-way coupling between a global anisotropic MHD model and an anisotropic ring current model, which allows us to study the global pattern of pressure anisotropy in the terrestrial magnetosphere more completely.

[68] The two-way coupling between Anisotropic BATS-R-US and the RCM is adopted from the coupling between BATS-R-US and the RCM. Since the RCM assumes isotropic pressure, both the total and parallel pressures along the closed field lines in the anisotropic MHD model are nudged toward the RCM pressure with the assumption that the pressures are constant along field lines.

[69] The two-way coupling between Anisotropic BATS-R-US and the CRCM is more sophisticated. For the CRCM to Anisotropic BATS-R-US coupling, by feeding Anisotropic BATS-R-US with the CRCM density and pressures at "minimum B" points on closed field lines, we calculate the density and pressures at "nonminimum B" points along closed field lines in Anisotropic BATS-R-US based on the relations (3), (4), and (5), which are obtained by Liouville's Theorem and based on a set of assumptions. For Anisotropic BATS-R-US to the CRCM coupling, in addition to the magnetic field information, the CRCM also uses the density and pressures from Anisotropic BATS-R-US to set boundary conditions.

[70] The coupled Anisotropic BATS-R-US and ring current models are validated through global magnetospheric simulations and compared to the standard coupled BATS-R-US and ring current models. In the idealized simulations, we find significantly increased nightside pressure and pressure gradient toward the Earth in the MHD solutions for both the RCM and the CRCM coupled anisotropic MHD cases than for the anisotropic MHD only case. However, compared to the corresponding isotropic MHD simulations, the RCM coupled anisotropic MHD gives less nightside pressure, while the CRCM coupled anisotropic MHD gives more nightside pressure. In the anisotropic MHD solutions, the pressure anisotropy in the inner magnetosphere is the largest for the CRCM coupled simulations, and the smallest for the RCM coupled simulations as expected. We also find that the inclusion of pressure anisotropy in the global MHD model that is coupled with the RCM or the CRCM brings the subsolar magnetopause and the bow shock toward the Earth, and the resulting magnetosheath is thinner. In addition, we find that the RCM or the CRCM coupled anisotropic MHD simulation produces a shorter tail, more compressed closed field lines on the nightside, and a much slower Earthward flow jet from the tail reconnection site, compared to the corresponding isotropic MHD simulations. The conclusions from the idealized simulations imply that pressure anisotropy plays an important role in controlling the magnetic field configuration and maybe some other physical processes in the global magnetosphere.

[71] In two geomagnetic storm simulations, we observe less ring current during the main and recovery phases produced by the anisotropic MHD model than by the isotropic MHD model for the CRCM coupled simulations. For the 2009 storm, the anisotropic MHD driven CRCM produces less anisotropic plasma for the ring current compared to the isotropic MHD driven CRCM does. For the comparisons with the satellite data, we see mostly improvements, but also drawbacks from the anisotropic MHD simulations compared to the isotropic MHD simulations. In particular, anisotropic MHD improves the magnetic field agreement with the Geotail data and the velocity agreement with the THEMIS A data a lot for the 2009 storm, meanwhile it predicts worse field line stretching as seen by the GOES satellites. In most cases, the CRCM coupled anisotropic MHD simulation and the two RCM coupled simulations produce competitive results. Moreover, for the RCM coupled simulations, the isotropic MHD case sometimes shows better match with the data than the anisotropic MHD case does. In our opinion, this reveals the importance of consistency between the global MHD model and the ring current model. The RCM assumes

isotropic pressure, so does the isotropic MHD model. In principle, the RCM coupled isotropic MHD model is more consistent than the RCM coupled anisotropic MHD model. This might also explain the incorrect tail tilt seen in the CRCM coupled isotropic MHD simulation in Figure 15, as the coupling between a isotropic MHD model with an anisotropic ring current model is less consistent.

Appendix A: Particle Distribution and Force Balance Along Field Lines

[72] Let us assume that the particle distribution at the "minimum B" point (represented by subscript "0") of a closed field line can be written as

$$f_0(\mathbf{v}_0) = \phi\left(\frac{v_{\perp 0}^2}{T_{\perp 0}} + \frac{v_{\parallel 0}^2}{T_{\parallel 0}}\right) \tag{A1}$$

where v is particle speed, T is temperature, and the subscript "$\perp$" and "$\parallel$" stand for the directions perpendicular to and along with the magnetic field, and ϕ is an arbitrary function of $v_\perp^2/T_\perp + v_\parallel^2/T_\parallel$. For bi-Maxwellian distribution, $\phi(x) = A\exp(-mx/2k)$; For bi-Kappa distribution, $\phi(x) = B(1+mx/(k(2\kappa-3)))^{-\kappa-1}$, or in terms of characteristic energy, $\phi(y) = B(1+my/(2\kappa))^{-\kappa-1}$ with $y = v_\parallel^2/E_{ch\parallel} + v_\perp^2/E_{ch\perp}$, where $E_{ch\parallel}$ and $E_{ch\perp}$ are parallel and perpendicular characteristic energy, respectively. Both A and B are normalization factors, m is particle mass, and k is Boltzmann constant.

[73] Liouville's theorem gives the particle distribution at an arbitrary "nonminimum B" point (represented by subscript "λ") as

$$f_\lambda(\mathbf{v}_\lambda) = f_0(\mathbf{v}_0(\mathbf{v}_\lambda)) \tag{A2}$$

To find $\mathbf{v}_0(\mathbf{v}_\lambda)$, we connect the components of $\mathbf{v}_0$ and $\mathbf{v}_\lambda$ through the conservation of the first adiabatic invariant as

$$\mu = \frac{mv_{\perp 0}^2}{2B_0} = \frac{mv_{\perp\lambda}^2}{2B_\lambda} \tag{A3}$$

and the conservation of energy with neglecting potential drop along the field line as

$$E = \frac{1}{2}mv_{\perp 0}^2 + \frac{1}{2}mv_{\parallel 0}^2 = \frac{1}{2}mv_{\perp\lambda}^2 + \frac{1}{2}mv_{\parallel\lambda}^2 \tag{A4}$$

where m is particle mass and B is magnetic field strength. From equation (A3) we obtain

$$v_{\perp 0}^2 = v_{\perp\lambda}^2\frac{B_0}{B_\lambda} \tag{A5}$$

which can be substituted into equation (A4) to get

$$v_{\parallel 0}^2 = v_{\perp\lambda}^2\left(1 - \frac{B_0}{B_\lambda}\right) + v_{\parallel\lambda}^2 \tag{A6}$$

Therefore,

$$f_\lambda(\mathbf{v}_\lambda) = \phi\left(\frac{v_{\perp\lambda}^2\frac{B_0}{B_\lambda}}{T_{\perp 0}} + \frac{v_{\perp\lambda}^2(1-\frac{B_0}{B_\lambda}) + v_{\parallel\lambda}^2}{T_{\parallel 0}}\right) \tag{A7}$$

Defining

$$T_{\perp\lambda} = \frac{T_{\perp 0}}{T_{\perp 0}/T_{\parallel 0} + B_0/B_\lambda(1 - T_{\perp 0}/T_{\parallel 0})} \tag{A8}$$

$$T_{\parallel\lambda} = T_{\parallel 0} \tag{A9}$$

the distribution function at "λ" can be written into the same form as the distribution function at "0" (equation (A1)):

$$f_\lambda(\mathbf{v}_\lambda) = \phi\left(\frac{v_{\perp\lambda}^2}{T_{\perp\lambda}} + \frac{v_{\parallel\lambda}^2}{T_{\parallel\lambda}}\right) \tag{A10}$$

We can obtain the number density at "0" and "λ" through

$$n_0 = \iiint_{\mathbf{v_0}} f_0(\mathbf{v}_0)\,d\mathbf{v}_0 = \iiint_{\mathbf{v_0}} \phi\left(\frac{v_{\perp 0}^2}{T_{\perp 0}} + \frac{v_{\parallel 0}^2}{T_{\parallel 0}}\right) d\mathbf{v}_0 \tag{A11}$$

and

$$n_\lambda = \iiint_{\mathbf{v}_\lambda} f_\lambda(\mathbf{v}_\lambda)\,d\mathbf{v}_\lambda = \iiint_{\mathbf{v}_\lambda} \phi\left(\frac{v_{\perp\lambda}^2}{T_{\perp\lambda}} + \frac{v_{\parallel\lambda}^2}{T_{\parallel\lambda}}\right) d\mathbf{v}_\lambda \tag{A12}$$

$f_0(\mathbf{v}_0)$ and $f_\lambda(\mathbf{v}_\lambda)$ are identical except that the velocities are scaled with different $\sqrt{T_\perp}$, given $T_{\parallel\lambda} = T_{\parallel 0}$. So the volumes wrapped by the distribution functions over velocity space, i.e., n_0 and n_λ, are different by a factor of $(\sqrt{T_{\perp 0}}/\sqrt{T_{\perp\lambda}})^2$, where the square accounts for the two perpendicular directions. Hence,

$$n_\lambda = \frac{T_{\perp\lambda}\sqrt{T_{\parallel\lambda}}}{T_{\perp 0}\sqrt{T_{\parallel 0}}}n_0 = \frac{T_{\perp\lambda}}{T_{\perp 0}}n_0 \tag{A13}$$

Then we can rewrite n_λ with the help of (A8) as

$$n_\lambda = \frac{n_0}{T_{\perp 0}/T_{\parallel 0} + B_0/B_\lambda(1 - T_{\perp 0}/T_{\parallel 0})} \tag{A14}$$

Finally, using $p_{\parallel 0} = n_0kT_{\parallel 0}$, $p_{\parallel\lambda} = n_\lambda kT_{\parallel\lambda}$, $p_{\perp 0} = n_0kT_{\perp 0}$ and $p_{\perp\lambda} = n_\lambda kT_{\perp\lambda}$, we can express the number density, the parallel and perpendicular pressures at "λ" as

$$n_\lambda = \frac{n_0}{p_{\perp 0}/p_{\parallel 0} + B_0/B_\lambda(1 - p_{\perp 0}/p_{\parallel 0})} \tag{A15}$$

$$p_{\parallel\lambda} = \frac{p_{\parallel 0}}{p_{\perp 0}/p_{\parallel 0} + B_0/B_\lambda(1 - p_{\perp 0}/p_{\parallel 0})} \tag{A16}$$

$$p_{\perp\lambda} = \frac{p_{\perp 0}}{(p_{\perp 0}/p_{\parallel 0} + B_0/B_\lambda(1 - p_{\perp 0}/p_{\parallel 0}))^2} \tag{A17}$$

The above relations, also given as equations (3), (4), and (5), agree with previous studies [*Spence et al.*, 1987; *Olsen et al.*, 1994; *Xiao and Feng*, 2006]. They are valid for any distribution function $\phi(x)$ with $x = v_\perp^2/T_\perp + v_\parallel^2/T_\parallel$ at the "minimum B" point of a closed field line.

[74] We now show that the pressures given by (A16) and (A17) satisfy the force balance condition along closed field lines in anisotropic MHD. The force parallel to a field line at an arbitrary point λ is given by

$$\mathbf{F}_{\parallel\lambda} = (p_{\parallel\lambda} - p_{\perp\lambda})B_\lambda\nabla_\parallel(B_\lambda^{-1}) + \nabla_\parallel p_{\parallel\lambda} \tag{A18}$$

We can write (A16) and (A17) as $p_{\parallel\lambda} = p_{\parallel 0}/g$ and $p_{\perp\lambda} = p_{\perp 0}/g^2$, where $g = (p_{\perp 0}/p_{\parallel 0} + B_0/B_\lambda(1 - p_{\perp 0}/p_{\parallel 0}))$. Substituting into the first term of (A18), we get

$$\begin{aligned}(p_{\parallel\lambda} - p_{\perp\lambda})B_\lambda\nabla_\parallel(B_\lambda^{-1}) &= \left(\frac{p_{\parallel 0}}{g} - \frac{p_{\perp 0}}{g^2}\right)B_\lambda\nabla_\parallel(B_\lambda^{-1}) \\ &= \frac{(gp_{\parallel 0} - p_{\perp 0})B_\lambda}{g^2}\nabla_\parallel(B_\lambda^{-1}) \\ &= \frac{(p_{\parallel 0} - p_{\perp 0})B_0}{g^2}\nabla_\parallel(B_\lambda^{-1})\end{aligned} \tag{A19}$$

while the second term of (A18) gives

$$\nabla_{\parallel} p_{\parallel\lambda} = -\frac{p_{\parallel 0}}{g^2} g'(B_\lambda^{-1}) \nabla_{\parallel}(B_\lambda^{-1}) = -\frac{(p_{\parallel 0} - p_{\perp 0}) B_0}{g^2} \nabla_{\parallel}(B_\lambda^{-1}) \quad \text{(A20)}$$

where we used the fact that B_λ is the only nonconstant variable in g along the field line. (A19) and (A20) cancel out, thus the net force $\mathbf{F}_{\parallel\lambda}$ is zero. The force balance condition is achieved.

[75] **Acknowledgments.** The authors thank Andrei Runov and the THEMIS team for providing the THEMIS data. The authors also acknowledge N. Ness at Bartol Research Institute, D. J. McComas at SWRI, K. Ogilvie at NASA GSFC and CDAweb for providing the IMF and solar wind data from ACE and WIND, S. Kakugun at STELAB Nagoya Univ., and CDAweb for providing the Geotail data, and H. Singer at NOAA SEC and CDAweb for providing the GOES data. The SYM-H data is taken from the World Data Center (WDC) for Geomagnetism, Kyoto. This work was supported by various research grants from NASA and NSF. The computing resources were provided by the NASA High-End Computing (HEC) Program through the NASA Advanced Supercomputing (NAS) Division at Ames Research Center.

[76] Masaki Fujimoto thanks Sorin Zaharia and another reviewer for their assistance in evaluating this paper.

References

Buzulukova, N., M.-C. Fok, A. Pulkkinen, M. Kuznetsova, T. E. Moore, A. Glocer, P. C. Brandt, G. Toth, and L. Rastatter (2010), Dynamics of ring current and electric fields in the inner magnetosphere during disturbed periods: CRCM–BATS-R-US coupled model, *J. Geophys. Res.*, *115*, A05210, doi:10.1029/2009JA014621.

De Michelis, P., I. A. Daglis, and G. Consolini (1999), An average image of proton plasma pressure and of current systems in the equatorial plane derived from AMPTE/CCE-CHEM measurements, *J. Geophys. Res.*, *104*, 28,615–28,624.

De Zeeuw, D., S. Sazykin, R. Wolf, T. Gombosi, A. Ridley, and G. Tóth (2004), Coupling of a global MHD code and an inner magnetosphere model: Initial results, *J. Geophys. Res.*, *109*, A12219, doi:10.1029/2003JA010366.

DeCoster, R. J., and L. A. Frank (1979), Observations pertaining to the dynamics of the plasma sheet, *J. Geophys. Res.*, *84*(A9), 5099–5121.

Fok, M., R. A. Wolf, R. W. Spiro, and T. E. Moore (2001), Comprehensive computational model of earth's ring current, *J. Geophys. Res.*, *106*(A5), 8417–8424.

Fok, M., T. E. Moore, P. C. Brandt, D. C. Delcourt, S. P. Slinker, and J. A. Fedder (2006), Impulsive enhancements of oxygen ions during substorms, *J. Geophys. Res.*, *111*, A10222, doi:10.1029/2006JA011839.

Glocer, A., M. Fok, X. Meng, G. Tóth, N. Buzulukova, S. Chen, and K. Lin (2013), CRCM + BATS-R-US two way coupling, *J. Geophys. Res. Space Physics*, *118*, 1635–1650, doi:10.1002/jgra.50221.

Hu, B., F. R. Toffoletto, R. A. Wolf, S. Sazykin, J. Raeder, D. Larson, and A. Vapirev (2010), One-way coupled OpenGGCM/RCM simulation of the 23 March 2007 substorm event, *J. Geophys. Res.*, *115*, A12205, doi:10.1029/2010JA015360.

Jordanova, V. K., J. U. Kozyra, A. F. Nagy, and G. V. Khazanov (1997), Kinetic model of the ring current—Atmosphere interactions, *J. Geophys. Res.*, *102*, 14,279–14,291.

Koren, B. (1993), A robust upwind discretisation method for advection, diffusion and source terms, in *Numerical Methods for Advection-Diffusion Problems*, edited by C. Vreugdenhil and B. Koren, p. 117–138, Vieweg, Braunschweig.

Liemohn, M. W. (2003), Yet another caveat to the Dessler-Parker-Sckopke relation, *J. Geophys. Res.*, *108*(A6), 1251, doi:10.1029/2003JA009839.

Lui, A., and D. Hamilton (1992), Radial profiles of quiet time magnetospheric parameters, *J. Geophys. Res.*, *97*, 19,325–19,332.

Lyon, J., J. Fedder, and C. Mobarry (2004), The Lyon-Fedder-Mobarry (LFM) global MHD magnetospheric simulation code, *J. Atmos. Sol. Terr. Phys.*, *66*, 1333–1350.

Meng, X., G. Tóth, M. W. Liemohn, T. I. Gombosi, and A. Runov (2012a), Pressure anisotropy in global magnetospheric simulations: A magnetohydrodynamics model, *J. Geophys. Res.*, *117*, A08216, doi:10.1029/2012JA017791.

Meng, X., G. Tóth, I. V. Sokolov, and T. I. Gombosi (2012b), Classical and semirelativistic magnetohydrodynamics with anisotropic ion pressure, *J. Comput. Phys.*, *231*, 3610–3622, doi:10.1016/j.jcp.2011.12.042.

Moore, T. E., M. Fok, D. C. Delcourt, S. P. Slinker, and J. A. Fedder (2008), Plasma plume circulation and impact in an MHD substorm, *J. Geophys. Res.*, *113*, A06219, doi:10.1029/2008JA013050.

Olsen, R. C., L. J. Scott, and S. A. Boardsen (1994), Comparison between liouville's theorem and observed latitudinal distributions of trapped ions in the plasmapause region, *J. Geophys. Res.*, *99*(A2), 2191–2203.

Pembroke, A., F. Toffoletto, S. Sazykin, M. Wiltberger, J. Lyon, V. Merkin, and P. Schmitt (2012), Initial results from a dynamic coupled magnetosphere-ionosphere-ring current model, *J. Geophys. Res.*, *117*, A02211, doi:10.1029/2011JA016979.

Phan, T.-D., G. Paschmann, W. Baumjohann, and N. Sckopke (1994), The magnetosheath region adjacent to the dayside magnetopause: AMPTE/IRM observations, *J. Geophys. Res.*, *99*(A1), 121–141.

Powell, K., P. Roe, T. Linde, T. Gombosi, and D. L. De Zeeuw (1999), A solution-adaptive upwind scheme for ideal magnetohydrodynamics, *J. Comput. Phys.*, *154*, 284–309.

Raeder, J., R. L. McPherron, L. A. Frank, S. Kokubun, G. Lu, T. Mukai, W. R. Paterson, J. B. Sigwarth, H. J. Singer, and J. A. Slavin (2001), Global simulation of the Geospace Environment Modeling substorm challenge event, *J. Geophys. Res.*, *106*, 381–395.

Ridley, A., T. Gombosi, and D. Dezeeuw (2004), Ionospheric control of the magnetosphere: Conductance, *Ann. Geophys.*, *22*, 567–584.

Rusanov, V. (1961), Calculation of interaction of non-steady shock waves with obstacles, *J. Comput. Math. Phys.*, *1*, 267–279.

Sheldon, R. B., and D. C. Hamilton (1993), Ion transport and loss in the Earth's quiet ring current 1. Data and standard model, *J. Geophys. Res.*, *98*(A8), 13,491–13,508.

Spence, H. E., M. G. Kivelson, and R. J. Walker (1987), Static magnetic field models consistent with nearly isotropic plasma pressure, *Geophys. Res. Lett.*, *14*(8), 872–875.

Spreiter, J., A. Summers, and A. Alksne (1966), Hydrodynamic flow around the magnetosphere, *Planet. Space Sci.*, *14*, 223–253.

Takahashi, K., and J. E. W. Hones (1988), ISEE 1 and 2 observations of ion distributions at the plasma sheet-tail lobe boundary, *J. Geophys. Res.*, *93*(A8), 8558–8582.

Toffoletto, F., S. Sazykin, R. Spiro, and R. Wolf (2003), Inner magnetospheric modeling with the Rice Convection Model, *Space Sci. Rev.*, *107*, 175–196.

Toffoletto, F., S. Sazykin, R. Spiro, R. Wolf, and J. Lyon (2004), RCM meets LFM: Initial results of one-way coupling, *J. Atmos. Sol. Terr. Phys.*, *66*, 1361–1370.

Tóth, G., et al. (2012), Adaptive numerical algorithms in space weather modeling, *J. Comput. Phys.*, *231*, 870–903, doi:10.1016/j.jcp.2011.02.006.

Walsh, A. P., C. J. Owen, A. N. Fazakerley, C. Forsyth, and I. Dandouras (2011), Average magnetotail electron and proton pitch angle distributions from Cluster PEACE and CIS observations, *Geophys. Res. Lett.*, *38*, L06103, doi:10.1029/2011GL046770.

Wolf, R. A., Y. Wan, X. Xing, J.-C. Zhang, and S. Sazykin (2009), Entropy and plasma sheet transport, *J. Geophys. Res.*, *114*, A00D05, doi:10.1029/2009JA014044.

Wu, L., F. Toffoletto, R. A. Wolf, and C. Lemon (2009), Computing magnetospheric equilibria with anisotropic pressures, *J. Geophys. Res.*, *114*, A05213, doi:10.1029/2008JA013556.

Xiao, F., and X. Feng (2006), Modeling density and anisotropy of energetic electrons along magnetic field lines, *Plasma Sci. Technol.*, *8*(3), 279.

Zaharia, S., M. F. Thomsen, J. Birn, M. H. Denton, V. K. Jordanova, and C. Z. Cheng (2005), Effect of storm-time plasma pressure on the magnetic field in the inner magnetosphere, *Geophys. Res. Lett.*, *32*, L03102, doi:10.1029/2004GL021491.